DOI: 10.24352/UB.OVGU-2017-060 TECHNISCHE MECHANIK, 34, 3-4, (2014), 166 – 189
submitted: October 15, 2013

Nanoindentation of Soft Polymers: Modeling, Experiments and Parameter Identification

Z. Chen, S. Diebels

Since the nanoindentation technique is able to measure the mechanical properties of extremely thin layers and small volumes with a high resolution, it also became one of the most important testing techniques for thin polymer layers and coatings. This work is focusing on the characterization of polymers using nanoindentation, which is dealt with by means of numerical computation, experiments and parameter identification. An analysis procedure is developed using the FEM based inverse method to evaluate the hyperelasticity and time-dependent properties. This procedure is firstly verified with a parameter re-identification concept. An important issue in this publication is to take into account the error contributions in real nanoindentation experiments. Therefore, the effects of surface roughness, adhesion force and the real shape of the tip are involved in the numerical model to minimize the systematic error between the experimental responses and the numerical predictions. The effects are quantified as functions or models with corresponding parameters to be identified.

1 Introduction

Nanoindentation testing is a fairly mature technique for hard metals, which uses the continuously sensed indentation depth combined with the measured applied force to determine the elastic modulus and the hardness of the test specimen. Since this technique is able to measure the local properties of extremely small volumes with a high resolution, it also became one of the primary testing techniques for the mechanical characterization of polymers and biological tissues. However, a lot of questions still need to be answered in order to enable a wide adaption of nanoindentation in polymers.

Most of the polymeric materials show highly elastic and viscous material behavior at the same time, called viscoelasticity. In the past decades, investigations of viscoelastic effects of polymeric materials using experimental testing, constitutive modeling and numerical computation have been published in e. g. (Holzapfel, 1996; Huber and Tsakmakis, 2000; Hartmann, 2002; Lion, 1996, 1998; Lubliner, 1985; Heimes, 2005). Therefore, creep of polymers during nanoindentation has the same effect on the measured force-displacement data as thermal drift. It is difficult to quantify the thermal drift as a linear function of time. A pronounced error may be included in the force-displacement data, if a long testing time is required in creep or relaxation loading histories. The main problem concerns the analysis method to characterize the viscoelasticity of a polymer by nanoindentation, which is still not resolved. The analysis procedure, which is used in most indentation instruments to determine the hardness and elastic modulus, is based on the Oliver & Pharr method (Oliver and Pharr, 1992, 2004). This analysis method assumes that the material behaves in an elastic-plastic manner and does not exhibit any time-dependent behavior or load rate dependence. This method is not applicable to a viscoelastic polymer. Furthermore, the measured hardness and elastic modulus are not sufficient to represent the rate-dependent properties. In order to identify the viscoelastic behavior of polymers by nanoindentation, two ways have been documented in the literature instead of the Oliver & Pharr method. The first method is based on analytical or semi-analytical solutions. These solutions are based on parameters of the respective viscoelastic model and represent the relationship between indentation force and displacement. The model parameters are then obtained by using the analytical functions in accordance with the experimental force-displacement data. Since the linear viscoelastic contact solutions are derived from the Hertz elastic contact theory according to the correspondence principle, this method is restricted as it only provides accurate identification for specific linear viscoelastic models under fixed experimental processes.

Besides, effects like non-linear friction, adhesion and surface roughness in nanoindentation experiments are not taken into account in the analytical solutions. The second method, the so-called inverse method, is performed by combining finite element method (FEM) modeling and numerical optimization. In this method, the objective function, which is the difference between experimental and numerical data, is minimized with respect to the model parameters using numerical optimization. The parameters of the constitutive models are identified as the optimized solution. Basic investigation on different optimization methods and inhomogeneous deformation fields of this inverse method have been presented in the literature, e. g. (Benedix et al., 1998; Kreissig, 1998; Mahnken, 2004). Huber et al. (Huber et al., 2002; Huber and Tyulyukovskiy, 2004; Klötzer et al., 2006; Tyulyukovskiy and Huber, 2006) have been the first to apply this method in indentation. They used neural networks to identify the material parameters from indentation experiments on metals. However, the inverse method is still a new topic regarding nanoindentation problems of polymeric materials. Hartmann (Hartmann et al., 2006) identified the viscoplastic model parameters with uniaxial tests and validated them using indentation tests. Rauchs (Rauchs et al., 2010; Rauchs and Bardon, 2011) employed a gradient-based numerical optimization method to identify viscous hyperelastic and elasto-viscoplastic material parameters. Guessasma (Guessasma et al., 2008) determined viscoelastic properties of biopolymer composite materials using the finite element calculation and nanoindentation experiments. Saux et al. (Le Saux et al., 2011) identified the constitutive model for rubber-like elasticity with micro-indentation tests. As the inverse method permits us to handle any material model with non-linear properties and to include additional effects in the numerical model, it is a useful new method to deal with the problems of identifying rate-dependent material properties by nanoindentation. Finally, as mentioned at the beginning, nanoindentation has a considerable advantage in determining local properties from continuously measured force-displacement data with a high resolution. Unfortunately, there are various problems that influence the actual material response during indentation, e. g. friction, adhesion, surface roughness, inhomogeneity and indentation process-associated factors. These problems result in a systematic error between the numerical and experimental results that often leads to even larger errors in the parameter identification (Rauchs and Bardon, 2011; Bolzon et al., 2004; Mata and Alcalá, 2004; Tyulyukovskiy and Huber, 2007). Therefore, quantification of these influences are indispensable to characterize the material accurately using the inverse method.

In this paper, the investigation on nanoindentation of soft polymers dealing with modeling, experiments and parameter identification is presented. An analysis procedure is developed with the FEM based inverse method to identify the equilibrium stress state and the viscous properties. This procedure is firstly verified with a parameters re-identification concept. An important issue in this article is to take into account the error contributions in real nanoindentation experiments. Therefore, the effects of surface roughness, adhesion force and the real shape of the tip are involved in the numerical model to minimize the systematic error between the experimental responses and the numerical predictions. The effects are quantified as functions or models with corresponding parameters to be identified.

2 Inverse Method

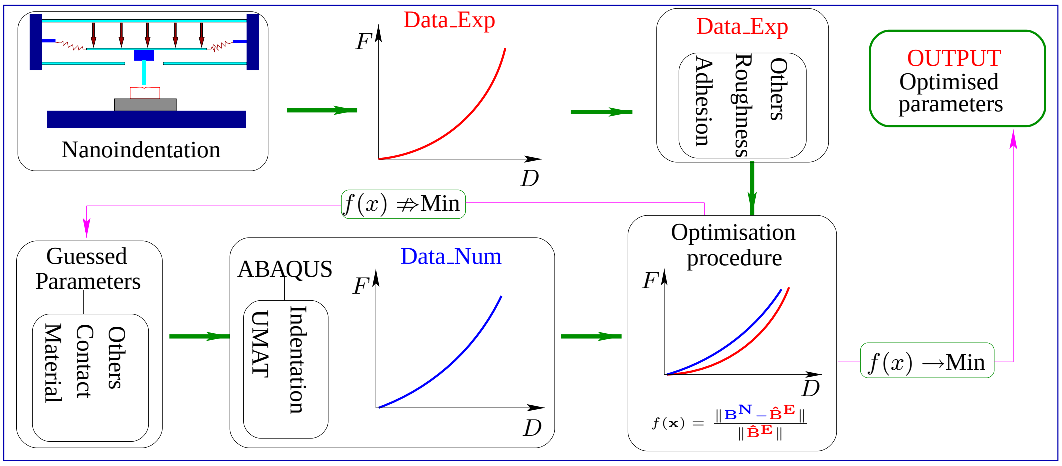

Figure 1: Flow-chart of the developed analysis procedure using FE based inverse method

The inverse method is a general framework that is used to convert observed measurements into information about a physical object or system that we are interested in. The experimental responses of a physical object or system, which is a prior information on a mathematically described model about this physical object or system, is treated as reference source to determine the model parameters in the inverse method. The finite element method (FEM) based inverse method is popular to use because it allows specimens with arbitrary shapes and physical processes with nonlinear nature and arbitrary loading conditions. This method is especially powerful if the material or structure properties are complex, e. g. nonlinear, heterogeneous and anisotropic. Since the indentation process on polymers involves strongly nonlinear contact mechanics as well as nonlinear time-dependent material properties, the FE based inverse method is chosen to develop a robust analysis procedure in this study.

Fig. 1 represents the flow-chart of the developed analysis procedure using the FEM based inverse method, which is a mixed experimental and numerical optimization problem. First of all, the force-displacement data obtained from nanoindentation experiments are used as reference source and are imported into an optimization procedure. The error contributions such as adhesion effects, surface roughness and other process associated factors are involved in the experimental data. The optimization procedure is developed combining the FEM code ABAQUS®/Standard with the mathematics tool MATLAB®. In the optimization procedure, the boundary value problem of nanoindentation is simulated in ABAQUS® taking into account the real geometry and real boundary conditions as in the experiments. In the numerical model, it is important to choose a suitable contact model between the indenter tip and the surface, a material model for the specimen and models predicting other affecting responses. It is the goal to determine the corresponding parameters of these models by this procedure. The principle of the method is to compare experimental force-displacement data with the computed results from the finite element model. Starting with guessed initial values, the models' parameters are iteratively updated by an optimization algorithm. The identification can then be formulated as an optimization problem where the objective function $f(x)$ to be minimized is an error function of the least squares type that expresses the difference between experimental measurements and the numerical predictions. The argument represents all model parameters, which have to be determined.

The choice of the optimization-based method for minimizing an objective function is a topic of interest. It is generally advised to use globally convergent optimization algorithms whenever possible. These algorithms are simulated annealing (Kirkpatrick et al., 1983; Goffe et al., 1994) or genetic algorithms (Schwefel, 1995; Deb, 2000), such as evolutionary algorithms, or deterministic algorithms like the Simplex method (Lawitts and Biggers, 1991; Lagarias et al., 1999). The gradient based algorithm is full of troublesome gradient calculation and the further drawback of local convergence. Genetic or evolutionary algorithms are globally convergent and are the only useful choice in a multi-objective optimization. Therefore, in this study, the genetic algorithm in MATLAB®'s Optimtool is used.

3 Virtual Experiments and Parameter Re-identification

In this present study, it is investigated how reliable the material parameters can be determined from the numerical optimization routine. In contrast to the traditional inverse method, virtual experimental data calculated by numerical simulations with chosen parameters replace the real experimental measurements. Such a procedure, which is called parameter re-identification was used in (Rauchs, 2006; Rauchs and Bardon, 2011) to validate the gradient-based material parameter identification routine. In this sense, the finite element code ABAQUS® is used as our virtual laboratory. An artificial random noise is superimposed on the virtual experimental data to make it more realistic and to check the stability of the identification procedure.

The numerical simulation of nanoindentation of polymer layers on a substrate, taking the real geometry into account, can be modeled by an axisymmetric two-dimensional model with a finite element code, e. g. ABAQUS®. The indenter is assumed to be a rigid body compared to the soft polymer layer. We define the indenter as an analytical rigid surface, in such a way that the indenter geometry can be modeled exactly with a smooth curve. In view of the strong nonlinear stiffness in contact problems, linear quadrilateral elements are used to get convergent results. Linear axisymmetric 4-node element type CAX4 is used for substrate since the deformation of substrate is very small and it is assumed that the substrate behaves in a linear elastic way. Considering the polymer layer in study as an incompressible material, the linear axisymmetric 4-node hybrid element type CAX4H in ABAQUS® is chosen. Since a very small change in displacement for incompressible material produces extremely large changes in pressure, a purely displacement-based solution is too sensitive to be useful numerically. ABAQUS® removes this singular behavior in the system by using hybrid elements, which are mixed formulation elements, using a mixture of displacement and stress variables with an augmented variational principle to approximate the equilibrium equations and compatibility conditions. The hybrid elements also remedy the problem of volume strain locking. A mesh convergence investigation has been performed by refining mesh gradually. It is essential that the density of nodes close to the indenter tip is high enough to consider the localized deformation of the layer. The nodes at the axis of symmetry are fixed in the horizontal direction, while those nodes at the bottom cannot move in the vertical direction. The geometry and boundary conditions of the spherical nanoindentation are illustrated in Fig. 2. Concerning the numerical treatment of the contact problem, the indenter is defined as master surface while the layer is defined as slave surface, both forming a contact pair. A contact formulation of finite-sliding interaction between a deformable and a rigid body in ABAQUS®/Standard is used to establish the frictionless contact model between indenter and layer. In this case, the formulation of the normal contact is used as a constraint for non-penetration which treats the normal contact as a unilateral constraint problem. The normal contact pressure cannot be calculated from a contact constitutive equation, but is then obtained as a reaction in the contact area and, hence, can be deduced from the constraint equations with the often used Lagrange multiplier method or the penalty method, for details please see (Wriggers, 2006).

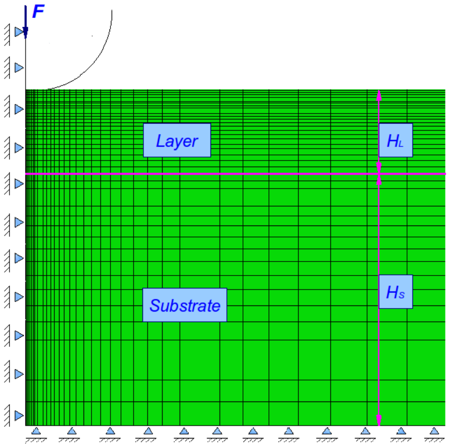

Figure 2: Sketch of FEM model of spherical nanoindentation

3.1 Hyperelasticity of Polymer Thin Film

3.1.1 Hyperelastic Models and the Corresponding Behaviors

We now restrict attention to isotropic and incompressible hyperelastic material models under isothermal regime, i. e. so-called perfectly elastic material models, because such hyperelastic models can well represent the behavior of the solid polymeric materials e. g. rubber-like materials (Holzapfel, 2001; Marckmann and Verron, 2005). With respect to the kinematics of continuum mechanics and the Helmholtz free-energy function Ψ, the 2^{nd} Piola-Kirchhoff stress tensor $\mathbf{S}$ and the Cauchy stress tensor $\mathbf{T}$ can be derived as (details see e. g. (Holzapfel, 2001, Chp. 6))

$$\mathbf{S} = -p\mathbf{C}^{-1} + 2\frac{\partial\Psi(\mathbf{C})}{\partial\mathbf{C}} = -p\mathbf{C}^{-1} + 2\frac{\partial\Psi}{\partial \mathrm{I}_{1\mathbf{C}}}\mathbf{I} + 2\frac{\partial\Psi}{\partial \mathrm{I}_{2\mathbf{C}}}(\mathrm{I}_{1\mathbf{C}}\mathbf{I} - \mathbf{C}), \tag{1}$$

$$\mathbf{T} = -p\mathbf{I} + 2\,\mathbf{B}\frac{\partial\Psi(\mathbf{B})}{\partial\mathbf{B}} = -p\mathbf{I} + 2\frac{\partial\Psi}{\partial \mathrm{I}_{1\mathbf{B}}}\mathbf{B} + 2\frac{\partial\Psi}{\partial \mathrm{I}_{2\mathbf{B}}}\mathbf{B}^{-1}. \tag{2}$$

Therefore, the constitutive equations of an isotropic and incompressible hyperelastic material under isothermal condition are given by eq. (1) and (2). $\mathbf{B}$and $\mathbf{C}$ are the left and right Cauchy Green deformation tensors, respectively. The constitutive equations are split into one part governed by the hydrostatic pressure p and the other part governed by the deformation of the material. There are numerous specific forms of strain-energy functions to describe the hyperelastic properties, whereas we only focus on three isotropic and incompressible hyperelastic models, namely the neo-Hooke, the Mooney-Rivlin and the Yeoh form:

$$\Psi_{\mathrm{NH}} = \mathrm{C}_{10}\,(\mathrm{I}_{1\mathbf{C}} - 3), \tag{3}$$

$$\Psi_{\mathrm{MR}} = \mathrm{C}_{10}\,(\mathrm{I}_{1\mathbf{C}} - 3) + \mathrm{C}_{01}\,(\mathrm{I}_{2\mathbf{C}} - 3), \tag{4}$$

$$\Psi_{\mathrm{Y}} = \mathrm{C}_{10}\,(\mathrm{I}_{1\mathbf{C}} - 3) + \mathrm{C}_{20}\,(\mathrm{I}_{1\mathbf{C}} - 3)^2 + \mathrm{C}_{30}\,(\mathrm{I}_{1\mathbf{C}} - 3)^3. \tag{5}$$

These forms are often used in the literature to model elastic properties of polymers. Ψ_{NH} involves only one single parameter and provides a mathematically simple and reliable constitutive model for the non-linear deformation behavior of isotropic rubber-like materials. It is physically-founded and includes typical effects known from non-linear elasticity within the small strain domain (Holzapfel, 2001; Marckmann and Verron, 2005; Rivlin, 1948). The free energy function Ψ_{MR} of the Mooney-Rivlin model is derived on the basis of mathematical arguments with consideration of symmetry (Mooney, 1940). It is often employed in the description of the non-linear behavior of isotropic rubber-like materials at moderate strain (Giannakopoulos and Triantafyllou, 2007; Holzapfel, 2001; Marckmann and Verron, 2005). Yeoh made the simplifying assumption that $\partial\Psi/\partial\mathrm{I}_2$ is zero and proposed a function Ψ_{Y} depending only on the first principle invariant. This phenomenological material model is motivated in order to simulate the mechanical behavior of carbon-black filled rubber showing a typical stiffening effect in the large strain domain (Holzapfel, 2001; Yeoh, 1990).

The parameters of the three models are chosen in such a way that the shear moduli at the reference configuration are the same for all methods, as listed in Table 1. It should be noted that the linearization of the three models at the small strain region yields the same Young's modulus $\mathrm{E} = 2\mu(1+\nu)$ ($\nu = 0.5$ is chosen for incompressible

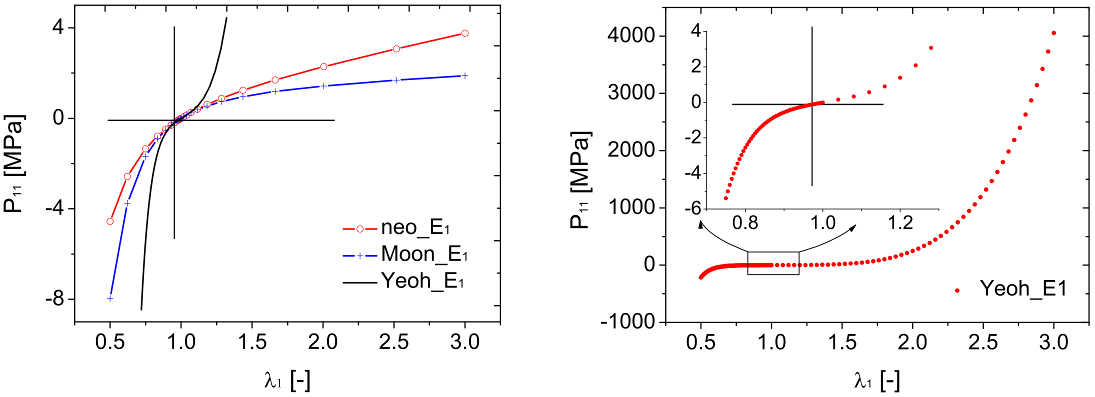

Figure 3: The 1^{st} Piola-Kirchhoff component over the stretch in the tension direction under uniaxial tension test: on the left side, the behavior of the neo-Hooke and Mooney-Rivlin models is shown and three models are compared; on the right side, the behavior of the Yeoh model is shown in the whole stretch range $0.5 \leq \lambda_1 \leq 3$

material) if Hooke's law is applied, i. e. the finite elasticity laws are set up in such a way that a uni-axial tension test yields the same tangent to the stress-strain curve in the origin, as shown in Fig. 3. As can be seen from the curves in Fig. 3, the elastic behavior of the Yeoh model displays the strongest non-linearity while the neo-Hooke model exhibits slight non-linear elasticity within the small strain domain. As expected in the parameter setting, the uniaxial tension tests of the three different hyperelastic models yield the same tangent to the stress-strain curve close to the origin $0.9 \leq \lambda_1 \leq 1.1$. Otherwise, the behavior of those models can be explicitly separated in the stretch range. The difference between the behavior of the Yeoh model and of the other two models is huge in the large strain domain. Therefore, the behavior of the three models under nanoindentation can be expected to be separated, too.

3.1.2 Results of Parameters Re-identification and Discussions

The friction effects between the indenter and the polymer layer as well as the friction between the polymer layer and the substrate are not taken into account. The algorithm requires bounds for each parameter as shown in Table 1. The computational cost can be reduced if narrow bounds are chosen. In general the choice of the bounds depends on the problem and the experience of the user. Also the choice of the starting vector has influence on the convergent speed to the optimal results. We investigates the evolution process of the material parameters of the Yeoh model with different starting vectors [0.1,0.5,1] and [0.1,1,1]. The result shows that the identified parameters with two different sets of initial vector are more or less the same. But the number of the generations used in the first case ([0.1,0.5,1]) is much lower than the number used in the second case ([0.1,1,1]). In this work, the starting vector [0.1,0.5,1] is used. The chosen parameters of the three material models are re-identified from the nanoindentation boundary value problem. Two maximum indentation depths, 5 μm and 40 μm, are chosen to investigate whether the accuracy of the identified parameters of the non-linear elastic models are dependent on the magnitude of the deformation under indentation. According to our former work (Chen and Diebels, 2012), the influence of the substrate is excluded if the maximum indentation depth is set to 5 μm i. e. u/H_L is smaller than 5%. One should keep in mind that the parameters of the three non-linear models are chosen in such a way that the linearization of the three models at small strain regime yields the same Young's modulus E. Therefore, as shown in Fig. 4, the relations of the force-displacement of the three models are more or less the same if the maximum indentation depth is restricted to 5 μm. This case can be considered as small deformation. If the maximum indentation depth is increased to 40 μm i. e. $u/H_L = 40\%$, the non-linear behavior of the hyperelastic models especially of the Yeoh form is fully developed under such finite deformation without excluding the influence of the substrate. The parameter identification is performed assuming that the properties of the substrate are known.

The re-identified parameters are listed in Table 1. Compared to the chosen values, the parameter C_{10} of the neo-Hooke model can always be identified perfectly independent on the degree of deformation and on the noise. For the Mooney-Rivlin model, a difference of the identified results at a maximum indentation depth of 5 μm and of 40 μm appears. C_{10} and C_{01} can be accurately identified only if the virtual experimental data at finite deformation is free of noise. For both cases of virtual experimental data with noise, the identified values of C_{10} and C_{01}

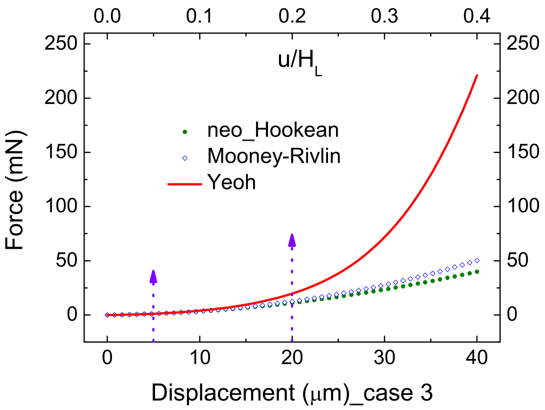

Figure 4: The response of the three hyperelastic models in nanoindentation simulation

Table 1: The re-identified parameters with maximum indentation depth 5 μm and 40 μm

Noise	**neo-Hooke**	**Mooney-Rivlin**			**Yeoh form**		
%	C_{10}	C_{10}	C_{01}	$C_{10}+C_{01}$	C_{10}	C_{20}	C_{30}
chosen value	0.6513	0.1640	0.4873	0.6513	0.6513	2.5870	5.0
bounds	(0.01;5)	(0.01;1)	(0.01;1)	—	(0.1;5)	(0.1;20)	(0.1;20)
initial	0.1	0.1	0.1	—	0.1	0.5	1
maximum indentation depth 5 μm							
0.0	0.6513	0.2060	0.4483	0.6509	0.6517	2.4920	7.7901
0.5	0.6533	0.2243	0.4316	0.6559	0.6733	0.9107	8.8551
2.0	0.6581	0.4375	0.2323	0.6698	0.6801	1.1695	1.4284
5.0	0.6640	0.5814	0.1097	0.6911	0.7096	0.1001	0.1022
sensitivity	3.045e4	3.048e4	3.157e4	—	3.052e4	3.377e2	7.290
maximum indentation depth 40 μm							
0.0	0.6513	0.1602	0.4903	0.6505	0.6515	2.5852	5.0026
0.5	0.6528	0.1845	0.4728	0.6573	0.6557	2.6019	4.9607
2.0	0.6578	0.2125	0.4547	0.6672	0.6721	2.6498	4.9230
5.0	0.6640	0.4722	0.2692	0.7414	0.7716	2.7291	4.5014
sensitivity	1.099e6	1.100e6	1.362e6	—	1.054e6	2.989e5	1.305e5

have a larger deviation from the chosen ones with the increament of the noise level. But the sum $C_{10} + C_{01}$ can always be identified exactly like the single parameter of the neo-Hooke model. The phenomenon is associated with the parameters coupling, as shown in Fig. 5. These findings also agree well with the theoretical analysis and experimental results reported in (Giannakopoulos and Panagiotopoulos, 2009; Giannakopoulos and Triantafyllou, 2007; Rauchs et al., 2010). The effect of parameters coupling decreases if the maximum displacement increases to 40 μm.

Now the focus lies on the identified results of the Yeoh model. For this model huge differences arise at small and finite deformation. At small deformation, except the first two parameters C_{10}, C_{20} are identified exactly when the virtual experimental data is free of noise. The identification of C_{30} is worse. If some noise is superimposed, C_{20} and C_{30} are worse to identify and finally they tend to the lower bounds. However, C_{10} can always be identified accurately. Attention should be paid to the results at large deformation, where all of the three parameters are identified exactly when the virtual experimental data is free of noise. In spite of the noise level increases up to 5% the biggest deviation of the identified parameters from the chosen parameters is less than 20%, which is still tolerable.

The reason for this behavior is related to the sensitivity of the indentation reaction force $\mathbf{F}$ with respect to the parameters (Mahnken and Stein, 1994). The sensitivity $\partial\mathbf{F}/\partial\kappa_i$ can be identified mathematically as follows:

$$\mathbf{F} := \mathbf{F}(\Re, \kappa_1, ..., \kappa_i, ..., \kappa_n) \tag{6}$$

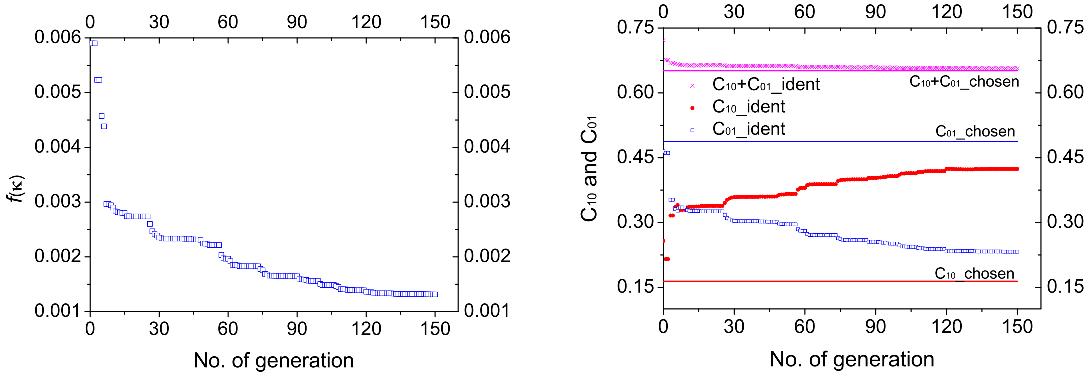

Figure 5: Parameters coupling during identification of parameters in Mooney-Rivlin model at small deformation with a noise level of 2.0%: the convergence of objective function (left), the evolution of both parameters (right)

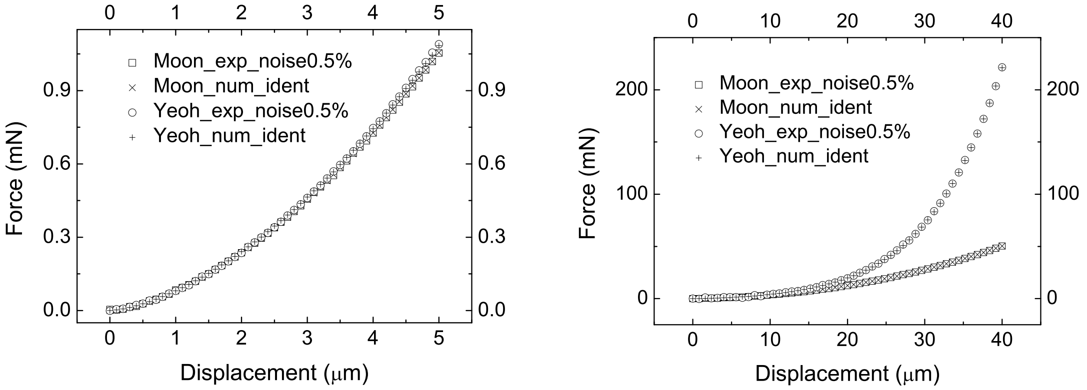

Figure 6: Comparison of virtual experimental data with 0.5% noise and numerical data with identified parameters: at small deformation (left), at finite deformation (right)

$$\frac{\partial \mathbf{F}}{\partial \kappa_i} \approx \frac{\|\mathbf{F}(\Re, \kappa_1, ..., \kappa_i + \delta\mu, ..., \kappa_n) - \mathbf{F}(\Re, \kappa_1, ..., \kappa_i, ..., \kappa_n)\|}{|\delta\mu|} \tag{7}$$

Herein, $\Re$ is the model of interest, $\delta\mu$ is the mutation increment or an increment of the parameter κ_i. Here we choose $\delta\mu$ as a relative value that is 10% of κ_i. The sensitivities with respect to κ_i are listed in Table 1: It shows that the more exactly re-identified parameters have a higher sensitivity than the parameters which are worse to identify. Although some parameters are not identified accurately, Fig. 6 shows good consistency of the virtual experimental data with 0.5% noise and the numerical data obtained with the re-identified parameters of Mooney-Rivlin and Yeoh models at both small and finite deformation. It should be pointed out that, even though the objective function is convergent to a minimum, the accuracy of each identified parameters of the polynomial-type hyperelastic models is not guaranteed. Similar findings are also included in the literature e. g. (Hartmann et al., 2001, 2003), that even the objective function is convergent, the material parameters are changing. In the present work, for Mooney-Rivlin model at small deformation, the contributions from C_{10} and C_{01} to the force-displacement relation cannot be divided. Because of this fact the force-displacement curve overlaps with the virtual experimental even though parameters coupling exists. For Yeoh model at small deformation, C_{20} and C_{30} are not identified successfully but the reaction force is not sensitive to them as shown in Table 1. That is to say, their contributions to the force-displacement results is much less than the contribution from C_{10}.

3.2 Identification of Hyperelasticity with Surface Roughness Effects

It is recognized from the experimental and the numerical investigations that the surface roughness has a significant influence on the force-displacement data at a small or a moderate indentation depth, which is comparable to the height of the surface asperities (Bobji et al., 1999; Berke et al., 2010; Kumar et al., 2006; Walter and Mitterer, 2008; Miller et al., 2008). In this part of work, the behavior of two hyperelastic soft polymers under nanoindentation is investigated numerically taking into account the effects of the surface roughness. The influence of the surface roughness is quantified phenomenological as a function of the sine curve parameters as well as of the indentation parameters.

3.2.1 Hyperelastic Material Models

Nanoindentation of two incompressible soft polymers by numerical simulation is considered here: polydimethylsiloxane (PDMS) 1:10 used in (Deuschle, 2008) and silicone rubber ELASTOSIL® RT 265 used in (Johlitz and Diebels, 2011). In the framework of finite strain continuum mechanics, the constitutive models of a nearly incompressible hyperelastic material can be derived by additively decomposing the Helmholtz free-energy function Ψ into the volumetric elastic part Ψ_{vol} and the isochoric elastic part Ψ_{iso}. For isotropic materials, it is further assumed that Ψ is expressed in terms of the principle invariant of the modified Cauchy-Green tensors $\bar{\mathbf{C}}$ or $\bar{\mathbf{B}}$.

$$\Psi = \Psi_{\mathrm{vol}}(J) + \Psi_{\mathrm{iso}}[\bar{I}_1(\bar{\mathbf{C}}), \bar{I}_2(\bar{\mathbf{C}})] = \Psi_{\mathrm{vol}}(J) + \Psi_{\mathrm{iso}}[\bar{I}_1(\bar{\mathbf{B}}), \bar{I}_2(\bar{\mathbf{B}})] \tag{8}$$

The strain invariant $\bar{I}_a (a = 1, 2)$ are the two modified principle invariants of $\bar{\mathbf{C}}$ and $\bar{\mathbf{B}}$. The constitutive equation of the 2^{nd} Piola-Kirchhoff stress tensor $\mathbf{S}$ in terms of the Jacobian J and the modified invariant $\bar{I}_1$, $\bar{I}_2$ (details see e. g. the textbook (Holzapfel, 2001, Chp. 6))

$$\begin{aligned} \mathbf{S} &= 2\frac{\partial \Psi(\mathbf{C})}{\partial \mathbf{C}} = \overline{\mathbf{T}}_{\mathrm{vol}} + \overline{\mathbf{T}}_{\mathrm{iso}} && (9) \\ &= J\frac{\partial \Psi_{\mathrm{vol}}(J)}{\partial J}\mathbf{C}^{-1} + 2\frac{\partial \Psi_{\mathrm{iso}}(\bar{I}_1, \bar{I}_2)}{\partial \bar{I}_1} : \frac{\partial \bar{I}_1}{\partial \mathbf{C}} + 2\frac{\partial \Psi_{\mathrm{iso}}(\bar{I}_1, \bar{I}_2)}{\partial \bar{I}_2} : \frac{\partial \bar{I}_2}{\partial \mathbf{C}}. && (10) \end{aligned}$$

According to (Deuschle, 2008; Johlitz and Diebels, 2011), the considered PDMS 1:10 will be modeled by a neo-Hooke model and the silicone rubber by a Mooney-Rivlin model (Simo and Taylor, 1982):

$$\begin{aligned} \Psi_{\mathrm{NH}} &= \Psi_{\mathrm{iso}}(\bar{I}_1) + \Psi_{\mathrm{vol}}(J) = \mathrm{C}_{10}\,(\bar{\mathrm{I}}_1 - 3) + \frac{1}{\mathrm{D}_1}[(\mathrm{J}-1)^2 + (\ln\mathrm{J})^2]/2, && (11) \\ \Psi_{\mathrm{MR}} &= \Psi_{\mathrm{iso}}(\bar{I}_1, \bar{I}_2) + \Psi_{\mathrm{vol}}(J) && (12) \\ &= \mathrm{C}_{10}\,(\bar{\mathrm{I}}_1 - 3) + \mathrm{C}_{01}\,(\bar{\mathrm{I}}_2 - 3) + \frac{1}{\mathrm{D}_1}[(\mathrm{J}-1)^2 + (\ln\mathrm{J})^2]/2. \end{aligned}$$

The initial shear modulus μ_0 and the initial compression modulus K_0 are related to the coefficients in the following way:

$$\begin{aligned} \mu_0 &= 2\frac{\partial \Psi_{\mathrm{iso}}}{\partial \bar{I}_a} \,|_{\bar{I}_a \to 1} = 2(\mathrm{C}_{10} + \mathrm{C}_{01}), && (13) \\ K_0 &= \frac{\partial^2 \Psi_{\mathrm{vol}}}{\partial J^2} \,|_{J \to 1} = \frac{2}{\mathrm{D}_1}. && (14) \end{aligned}$$

The compressibility parameter D_1 can be interpreted as a penalty parameter that enforces incompressibility if small values are chosen for D_1. The chosen parameters are listed in Table 2. In this study, D_1 of the silicone rubber is very small and hence it is not taken into account during the procedure of the parameters identification.

Table 2: Chosen material models and parameters of the indented polymers

Materials	**Chosen models**	**Parameters**			**Shear modulus**
PDMS	neo-Hooke	C_{10} 0.662 MPa	D_1 0.255 MPa		μ_0 1.324MPa
Silicone Rubber	Mooney-Rivlin	C_{10} 0.111 MPa	C_{01} 0.039 MPa	D_1 0.001MPa	μ_0 0.300 MPa

3.2.2 Parametric Investigation of Surface Roughness Effects

Generally speaking, a 3D model is necessary to represent the inhomogeneous properties of the realistic surface topography. However, the computing time occupies a large part in the inverse method and is, as a consequence, a key problem of the method. This often results in a trade-off between the computing cost and the quality of the numerical model. For instance, a 2D plane model or an axisymmetric model is used most commonly to save the computing cost. A plane strain modeling assumption is preferred, because the commonly real surface topography has a lack of axisymmetry and the position of the indenter can be set randomly on the rough surface in the plane strain model. The used spherical indenter with radius of 100 nm can be assumed to be a rigid body compared to the soft polymers. The geometrical size of the polymer sample is 2 $\mu m \times 2$ μm, which is sufficiently large to obtain a homogeneous stress distribution at the bottom and on the side boundaries of the model. The maximum indentation depth is 50 nm, which is limited to only 2.5% of the layer thickness. Therefore, the influence of the substrate and the friction between the indenter and the layer can be neglected according to (Chen et al., 2011).

The surface roughness effects are investigated numerically based on a phenomenological approach. A simple representation of the surface is chosen considering only a one-level of protuberance-on-protuberance profile described by a sine function $f(x) = H \sin \frac{2\pi}{\lambda} x$. Although this simplest model is only a regular wavy surface, it is the preferred model for us to perform the parametric investigation of the surface roughness effects. Moreover, most man-made surfaces such as those produced by grinding or machining, have a pronounced ”lay”, which may be modeled to a first approximation by this sinusoidal profile (Johnson, 1985). The parameters of the sinusoidal surface profile as well as the indentation geometric parameters are illustrated in Figure 7: the wave length λ, the roughness asperity height H, the spherical radius R and the indentation depth u. The whole indented sample surface, not only the part just under the indenter, is represented by the sinusoidal profile. This means that the influence of the interaction between the neighboring asperities of the real surface roughness is also taken into account. It has been shown experimentally that the influence of the surface roughness is dependent on the asperity shape (Berke et al., 2010). A large range of roughness asperity shapes from relatively sharp to smooth geometries is obtained by varying the asperity height $H = [5nm \cdots 50nm]$ and by varying the wave length $\lambda = [5nm \cdots 200nm]$.

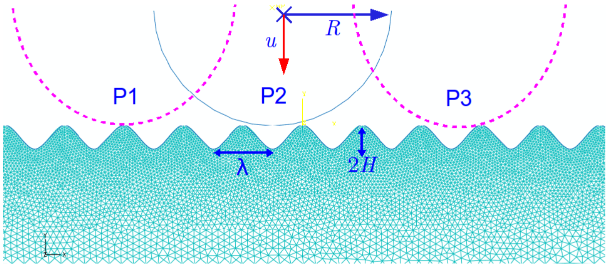

Figure 7: The mesh configuration of the one-level protuberance-on-protuberance profile

A parametric investigation is performed to study the dependence of the surface roughness effects on the roughness profile. It is first focused on varying the wave length λ from 5 nm to 200 nm with an invariant asperity height of 20 nm. The results show that the surface roughness can have a twofold effect resulting in either higher or lower contact stiffness. This twofold effect depends on the indentation position once the wave length increases to be comparable to the indenter radius and does not depend on the material. As shown in Figure 7, the three indentation positions are noted as P1, P2 and P3, denoting the indentation performed on the top, in a roughness valley and between the valley and the top respectively. The force-displacement data of the PDMS with low ratio λ/H are shown in Figure 8. The surface roughness has an effect resulting in much lower contact stiffness especially at the very beginning of the indentation. A physically sound reason can be the response of the extremely sharp asperity, which decreases the material stiffness. The criteria to remove the surface roughness effect suggested in (Jiang et al., 2008) by using a sufficiently large spherical indenter, has no use in this case. Nevertheless, the surface roughness effect on the force-displacement curve can be removed if a new initial indentation point is defined as shown in Figure 8. The initial contact point between indenter and surface can be re-defined to throw off the contact part in which the contact stiffness is nearly zero. The surface roughness effect decreases with an increasing wave length up to 50 nm. The roughness effect depends on the indentation position if the wave length is larger than 50 nm as shown in Figure 9. It can be seen explicitly that the surface roughness results in higher contact stiffness if the indentation is placed in a roughness valley and a lower stiffness if an asperity top is indented. This discovery has the same results as documented in (Berke et al., 2010). In the real nanoindentation test it is difficult to choose the indentation position neither in the valley or on the top. Therefore, it is reasonable to perform a sufficiently large number of indentations on various positions with statistical distribution. It is a good choice to take the mean value of the data with a reasonable discreteness in order to decrease the surface roughness effect. For instance, we can

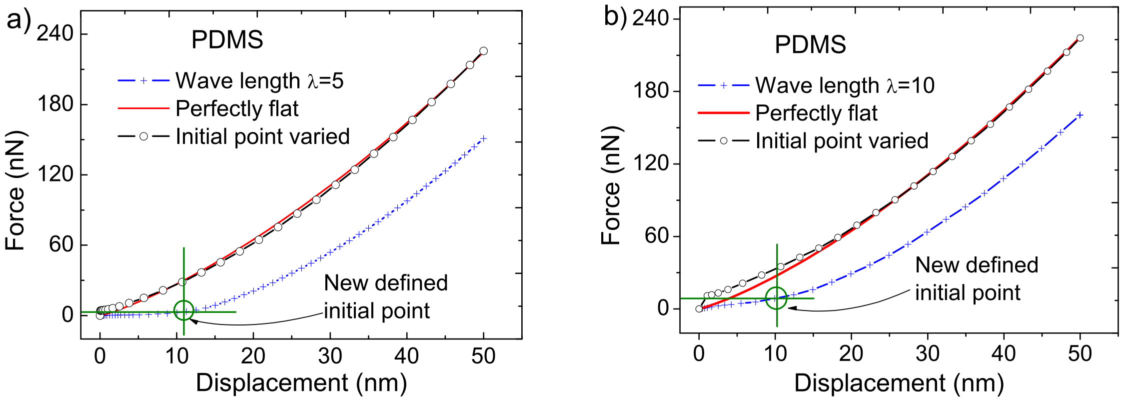

Figure 8: The force-displacement data obtained from indentation on flat surface and regular rough surface of PDMS, with a varying wave length: a) $\lambda = 5\ nm$; b) $\lambda = 10\ nm$. **Remark**: The new initial point of the force-displacement data is defined by a threshold of the measured reaction force that the reaction force is able to be measured. This is the usual way to define the initial contact of indents and surface in real experiments.

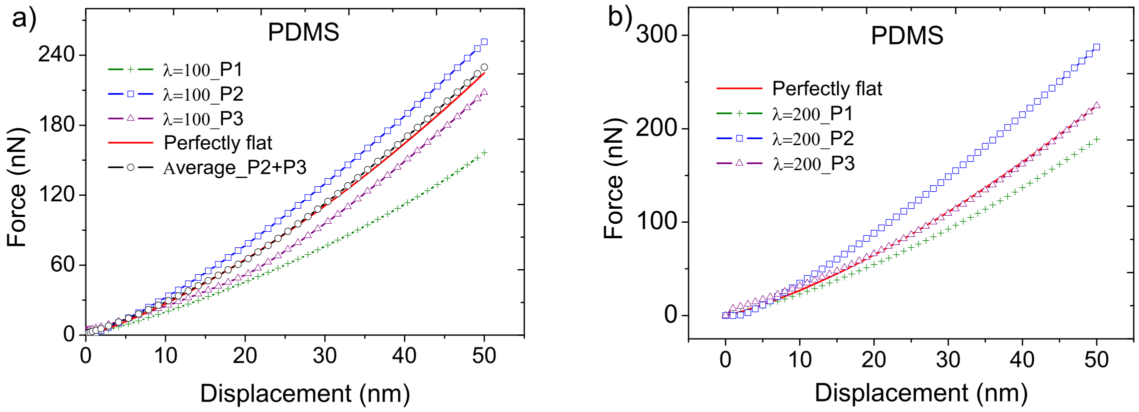

Figure 9: The force-displacement data obtained from indentation on flat surface and regular rough surface of PDMS, with a varying wave length: a) $\lambda = 100\ nm$; b) $\lambda = 200\ nm$

take the mean values "$\lambda = 100$_P2 & P3" in Figure 9 a) and "$\lambda = 200$_P1 & P3" in Figure 9 b) as the measured force-displacement data. We can also find similar conclusions in experimental as well as numerical investigations on hard metals in (Walter et al., 2007; Walter and Mitterer, 2008; Bouzakis et al., 2003).

The dependence of the surface roughness effect on the asperity height is investigated in the second step. In this case, the wave length is firstly fixed to 50 nm while the asperity height varies in a physically sound range from 5 nm to 50 nm. As the surface roughness has the same influence for the two investigated materials, only the results of the silicone are shown in Figure 10 in this time. The surface roughness has an effect on the force-displacement data depending on the ratio of the asperity height to the indentation depth H/u. The influence of the surface roughness in the force-displacement curve is negligible when H/u is sufficiently small, e. g. 1:10 (Figure 10 a)). The indentation result on a perfectly flat surface can still be used to approximate the measured data indented on a rough surface while the ratio H/u is below 1:3 (Figure 10 b)). A similar finding was also obtained by Donnelly et al. (Donnelly et al., 2006) in an experimental investigation of the indentation on cancellous bone. Nevertheless, the surface roughness effect results in decreasing contact stiffness of approximately 50% lower if the indentation depth is identical to the asperity height (Figure 10 c)).

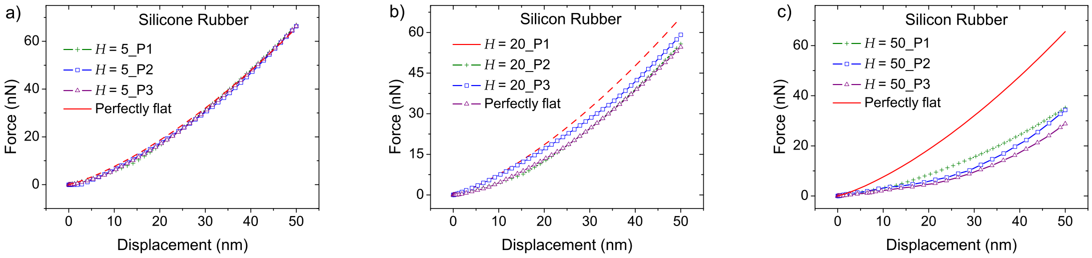

Figure 10: The force-displacement data obtained from an indentation on a flat surface and a regular rough surface of silicone rubber with varying asperity height: a) $H = 5\,nm$; b) $H = 20\,nm$; c) $H = 50\,nm$

Table 3: The identified parameters and their deviation compared with the chosen values listed in parentheses: indentation on a regular surface roughness

Virtual experimental data	**Identified parameters**		**Evaluated**
	C_{10}	D_1/C_{01}	μ_0
PDMS			
bounds	(0.01;1)	(0.01;1)	—
initial	0.05	0.05	—
Wave length $\lambda = 5$	0.2941 (-55.57%)	0.1001 (-60.78%)	0.5882 (-55.57%)
Initial point varied $\lambda = 5$	0.6288 (-5.02%)	0.2182 (-14.43%)	1.258 (-5.02%)
$\lambda = 100$_P1	0.6908 (+4.35%)	0.9818 (+285.02%)	1.382 (+4.35%)
Average_P2+P3 $\lambda = 100$	0.6740 (+1.81%)	0.2476 (-2.90%)	1.348 (+1.81%)
Silicone Rubber			
$H = 5$_P2	0.1017 (-8.38%)	0.0429 (+10.00%)	0.2889 (-3.60%)
$H = 20$_P2	0.0605 (-45.50%)	0.0769 (+97.18%)	0.2748 (-8.40%)
$H = 50$_P2	0.0318 (-71.32%)	0.0265 (-32.05%)	0.1167 (-61.11%)

3.2.3 Results and Discussion of Parameters Re-identification

The surface roughness effects are further quantified by the parameters re-identification. The virtual experimental data shown in Figures 8, 9 and 10 represent the indentation results obtained with the regular surface roughness model. The numerical data are the simulation results of the indentation on a perfectly flat surface with an arbitrary set of material parameters. All of the other geometrical parameters and of the boundary value problems of the virtual experimental setup and the numerical model are identical. The comparison of the identified parameters with the chosen values can be used to quantify the surface roughness effects. As it is described in Section 3.1.2, the bounds and the initial values of the model parameters are required within the identification procedure. The same bounds and the same initial values, which are listed in Table 3, are set for all the parameters to test the convergence. The identified parameters and the corresponding deviation are compared with the chosen values as shown in Table 3. The identified parameters C_{10} and D_1 of the neo-Hooke model are about 60% lower than the chosen values due to the effects of surface roughness with a wave length of 5 nm. It is worth to note that C_{10} and D_1 are accurately identified if a new initial point is defined to remove the surface roughness effects. The effects result in a much larger identified D_1 if the experiments are performed on the top of the asperity with a wave length of 100 nm. Nevertheless, if the virtual experimental data is replaced by the mean value of the indentation results on different positions, C_{10} and D_1 are exactly identified for the neo-Hooke model. The two parameters C_{10} and C_{01} of the Mooney-Rivlin model are accurately identified if the surface roughness possesses a low asperity height of 5 nm. The surface roughness with the asperity height of 20 nm leads to deviations of -45.50% and +97.18% for C_{10} and C_{01} respectively. But the evaluated initial shear modulus μ_0 using the identified parameters has an acceptable deviation from the reference value. The surface roughness effects can be neglected with respect to the results shown in Figure 10 b) and w. r. t. to the evaluated shear modulus μ_0. The existing parameters coupling is the main reason to cause a big deviation to the identified C_{10} and C_{01}. The surface roughness has an effect on the evaluated μ_0 resulting in a 61.11% lower value.

3.3 Viscoelasticity at Small Deformation

Viscoelasticity is another important property of polymeric materials. In this part of the work, we focus on identification of the viscoelastic model parameters from nanoindentation of polymer layers with various loading histories using the developed FEM based inverse procedure. A well known 3D linear viscoelastic model for small strain is taken into account (Lubliner, 1985). The incompressibility is expressed by splitting the deformation of the material into a deviatoric part and a volumetric part. Experimental investigations have shown that in many cases viscoelastic behavior is mainly related to the deviatoric part of the deformation (Kaliske and Rothert, 1997). The Cauchy stress tensor $\boldsymbol{\sigma}$ is expressed by

$$\boldsymbol{\sigma} = \boldsymbol{\sigma}_{eq} + \boldsymbol{\sigma}_{neq} = K(\mathrm{tr}\boldsymbol{\varepsilon})\mathbf{I} + 2\mu\boldsymbol{\varepsilon}^D + \sum_{j=1}^{n} 2\mu_e^j \boldsymbol{\varepsilon}_e^{j^D}, \tag{15}$$

with a linear evolution equation

$$\dot{\boldsymbol{\varepsilon}}_i^{j^D} = \frac{1}{r^j}\left(\boldsymbol{\varepsilon}^D - \boldsymbol{\varepsilon}_i^{j^D}\right). \tag{16}$$

Here, $\boldsymbol{\varepsilon}_e^{j^D} = \boldsymbol{\varepsilon}^D - \boldsymbol{\varepsilon}_i^{j^D}$. K and μ are the bulk modulus and shear modulus, respectively. $\boldsymbol{\varepsilon}^D$ is the deviatoric strain tensor. $\boldsymbol{\varepsilon}_i^{j^D}$ is the so-called deviatoric internal variable, which represents the viscous strain of the dashpot in the j^{th} Maxwell element. The relaxation time of each Maxwell element is given by $r^j = \eta^j/2\mu_e^j$. The FEM model of nanoindentation on polymer layer described in Section 3 for the parameter re-identification of hyperelasticity is used again to identify the viscoelasticity.

In the virtual experiments, three Maxwell elements are chosen with the corresponding parameters listed in Table 4. The displacement controlled nanoindentation tests with three kinds of relaxation paths are chosen to identify the model parameters, as shown in Fig. 11 and 13. It is aimed to investigate whether the multi-parameters' identification of the considered viscoelastic model depends on the loading history in nanoindentation. First of all, we focus on the identified results obtained from the two single step relaxation tests, which reach the same maximum indentation depth after a loading time of 0.1 s (Fig. 11 (left)) and of 1 s (Fig. 11 (right)). These two loading times are in the same decade with the relaxation time r^1 and r^2, respectively. The holding times of the two loading cases are kept the same as 30 s. Since the real model parameters are unknown in the traditional inverse method, a close match between the virtual experimental data and the prediction of the numerical model is the only way to judge the accuracy of the parameters identification. Fig. 12, left, shows the results of the single step relaxation with a loading time of 0.1 s. A close match between the virtual experimental data and the numerical results can be seen. Indeed, the match of the numerical data obtained with the parameters identified from the relaxation test with a loading time of 1 s is preferred except the force at $t = 0.1$ s. A deviation of 17% at this point can be seen from Fig. 12. Fig. 12, right, shows the comparable results of the relaxation test with a loading time of 1 s. The matches between the virtual experimental data and the numerical data obtained with both loading cases in Fig. 11 are great. According to the traditional way of judgment, we are confident to point out that the parameters identified from the two relaxation test should be accurate. The advantage of parameter re-identification allows us

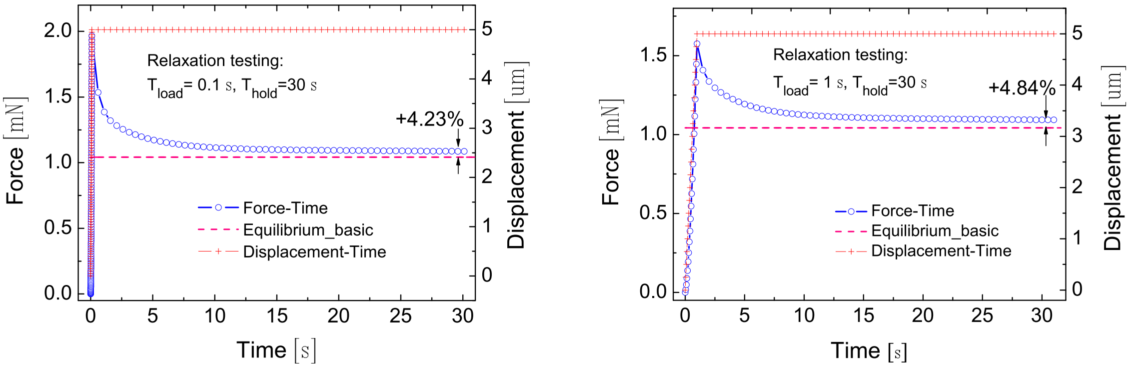

Figure 11: The loading history chosen for parameters identification and the corresponding force plotted at each time increment: single step relaxation with a loading time of 0.1 s (left) and with a loading time of 1 s (right)

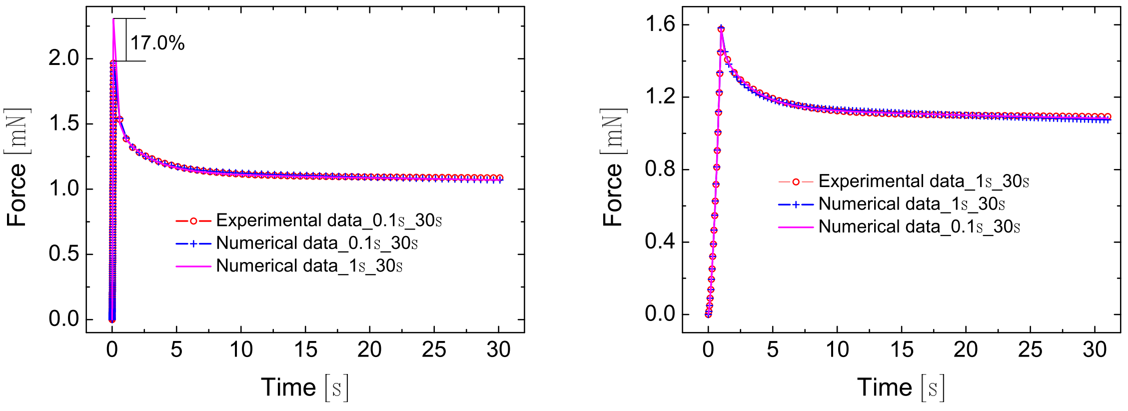

Figure 12: Comparison of the virtual experimental data with numerical simulation of a single step relaxation test: with a loading time of 0.1 s (left); with a loading time of 1 s (right). **Remark**: herein, Numerical data_0.1s_30s and Numerical data_1s_30s are the numerical simulation results with the parameters identified from the single step relaxation test with a loading time of 0.1 s and 30 s respectively

verifying the most often used way of judgment. The relative errors listed in Table 4 of the re-identified parameters with respect to the chosen values yield a contrary conclusion. In the relaxation test with a loading time of 0.1 s, the shear modulusμ_e^3 and the relaxation times r^2 and r^3 are not accurately identified that the deviation of μ_e^3 is as high as 121.60%. In the relaxation test with a loading time of 1 s, the shear moduli μ_e^1, μ_e^3 and the relaxation times r^1, r^2 are worse identified that the identified μ_e^1 is 147.04% greater than the chosen value. Therefore, in the case of multi-parameters identification, the perfect match between the virtual experimental data and the numerical prediction does not guarantee the accurate identification of each parameters. It seems that the identification of the shear moduli μ_e^j and the relaxation times r^j of the Maxwell elements are strongly dependent on the loading part of the relaxation tests. The reason may be that the sensitivity in eq. (7) of the reaction force with respect to the model parameters are different in various loading histories. These worse identified parameters have only a slight contribution to the reaction force due to a small sensitivity. This should also be the reason of the deviation of 17% in the force values shown in the left diagram of Fig. 12. The multistep relaxation paths contains seven single step relaxations with a loading time of 1 s and a 20 s holding stage as shown in Fig. 13, left. Fig. 14, left shows an extremely good match between the virtual experimental data and the numerical simulation using the same multi-step relaxation paths. Indeed, if the simulation is performed with the parameters identified from both single step relaxation tests, the deviation is still acceptable. In contrast to that, the relative errors of the parameters identified from multistep relaxation testing in Table 4 show absolutely not an optimistic result for all of the seven parameters compared with the chosen values. The basic elasticity is accurately captured by the multistep relaxation testing.

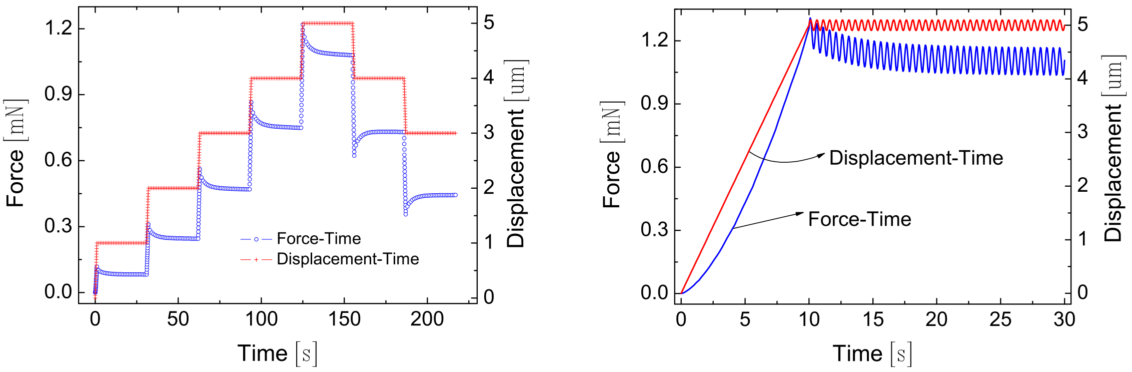

Figure 13: The loading history chosen for parameters identification and the corresponding force plotted at each time increment: multistep relaxation (left) and sinusoidal oscillatory (right) testing

Table 4: Re-identified parameters and their deviations compared with the chosen values for viscoelastic model being used. **Remark**: numbers in bold and italic font are those, whose absolute value is smaller than 20%.

Parameters	μ	μ_e^1	μ_e^2	μ_e^3	r^1	r^2	r^3
Chosen	1.3 MPa	0.8MPa	0.4MPa	0.1MPa	0.2s	3s	100s
Relax ($\mathrm{T_{load}} = 0.1\mathrm{s}$)	1.2325	0.7435	0.4030	0.2216	0.1869	2.0467	49.2780
	-5.19%	***-7.06%***	***+0.75%***	+121.60%	***-6.55%***	-31.78%	-50.72%
Relax ($\mathrm{T_{load}} = 1\mathrm{s}$)	1.2596	1.9763	0.4764	0.1732	0.0461	2.7307	58.9804
	-3.11%	+147.04%	***+19.10%***	+73.20%	-76.95%	***-8.98%***	-41.02%
Multistep	1.3238	0.3582	0.5762	0.1066	0.1857	1.6686	42.8211
	+1.83%	-55.23%	+44.05%	***+6.60%***	***-7.15%***	-44.38%	-57.18%
Oscillatory	1.2397	0.5914	0.4971	0.1536	0.2038	1.3184	64.0938
	-4.64%	-26.08%	+24.28%	+53.60%	***+1.90%***	-56.05%	-35.91%

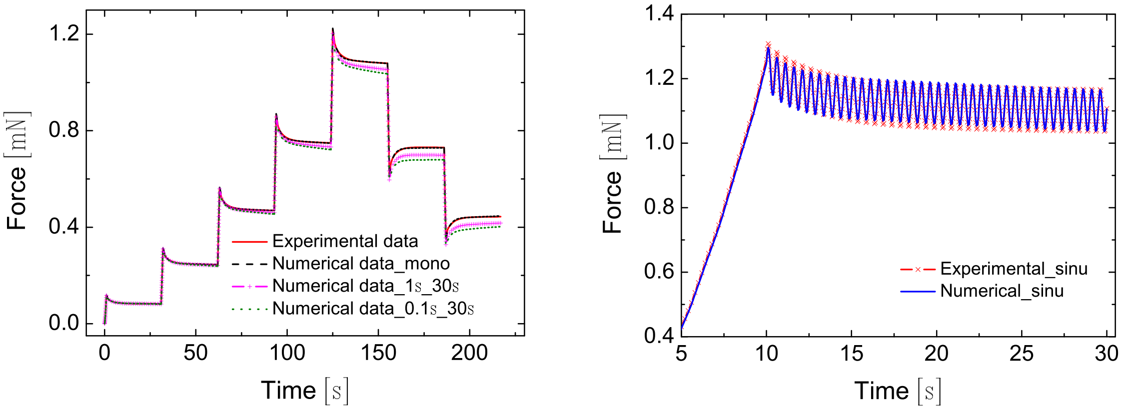

Figure 14: Comparison of the virtual experimental data with numerical simulation: multistep relaxation testing (left); sinusoidal oscillatory testing (right). **Remark**: herein, Numerical_mono and Numerical_sinu are numerical data obtained with the parameters identified from multistep relaxation and sinusoidal oscillatory testing respectively

Although the multistep relaxation test is composed with several single step relaxations, the identification results are really different from the results of the single step relaxation. The sinusoidal oscillatory test is performed with a 10 s ramping stage up to the maximum indentation depth 5 μm followed with a 20 s sinusoidal oscillatory loading. The sine function is designed with a frequency of 2 Hz and with an amplitude of 0.1 μm and is simulated in ABAQUS® with a step-size of 0.05 s. The comparison between the virtual experimental data and the numerical results is presented by the diagram in Fig. 14, right. These two curves overlap each other. A similar good result can also be seen in Table 4 except the identified value of μ_e^3 and r^2. Compared with the single step relaxation and the multistep relaxation testing, the parameters identified by the sinusoidal oscillatory loading history yield more harmonious results. The identified value of the longest relaxation time r^3 is much better than the results in other loading histories.

As a conclusion of this part of work, the parameters to be identified in the used viscoelastic model can be split into two sets: one set contains the shear modulus μ of the extra spring governed by the basic elasticity; the other set contains the shear moduli μ_e^j and the relaxation times r^j of the Maxwell elements governed by the viscoelastic behavior. Usually, the basic elasticity can be captured with a single step relaxation test with a sufficient long holding time. However, for the real polymers with a relaxation time of several months, it is effective to use the multistep relaxation testing to approximate the basic elasticity. It is found that the identification of the parameters in the Maxwell-elements is dependent on the relaxation paths. A suitable path which can address all the material parameters in this linear viscoelastic model is interesting for further investigation. Furthermore, the identified results of each loading paths show that the optimal parameters depend in a certain manner on each other. Therefore, similar to the investigation of elastic-plastic models to predict the inhomogeneous stress-strain fields in (Kreissig et al., 2001) and homogeneous stress-strain states in (Krämer et al., 2013), a description of parameters' correlation in indentation will be helpful in evaluating the modeling of material behaviors.

4 Real Experiments and Parameter Identification

The developed inverse procedure, which has been efficiently applied to re-identify the hyperelastic and viscoelastic models above, will be extended to characterize polymers from real nanoindentation tests. Silicone rubber, which can be assumed to be an isotropic elastomer, is chosen to be investigated. According to the experimental behavior in the obtained force-displacement data, a finite strain viscoelasticity model is required to predict the responses with consideration of adhesion effects. The parameters of the viscoelastic constitutive model and the adhesive contact model can then be identified by matching the response of the numerical model with the experimental force-displacement curves. The real geometry of the Berkovich tip (Fischer-Cripps, 2004) is taken into account to minimize the systematic error between the numerical model and the experiments.

4.1 Nanoindentation Experiments

The silicone rubber ELASTOSIL® RT 625 is produced by WACKER Chemie GmbH in Germany. The final specimen is of cylindrical shape with a diameter of 10 mm and a thickness about 2.02 mm. The surface roughness characterization is performed by scanning electron microscopy (SEM) and the In-Situ SPM Imaging mode of the Hysitron® indenter[1]. The two-dimensional optical analysis in Fig. 15 (left) clearly shows a perfectly smooth surface in the micron range. The local surface roughness obtained from the In-Situ SPM imaging is illustrated in Fig. 15 (right) and results in a RMS value of around 12 nm, which is not comparable to a maximum indentation depth of 3 μm during indentation. The characterized smooth surface implies two side-effects: on the one hand, it guarantees that the influence of the surface roughness is negligible according to results in the part 3.2; on the other hand, adhesion forces are very likely to be present, as there is a contact between two very smooth surfaces. Hence, the adhesion effects may have a potential influence on the measured force-displacement data.

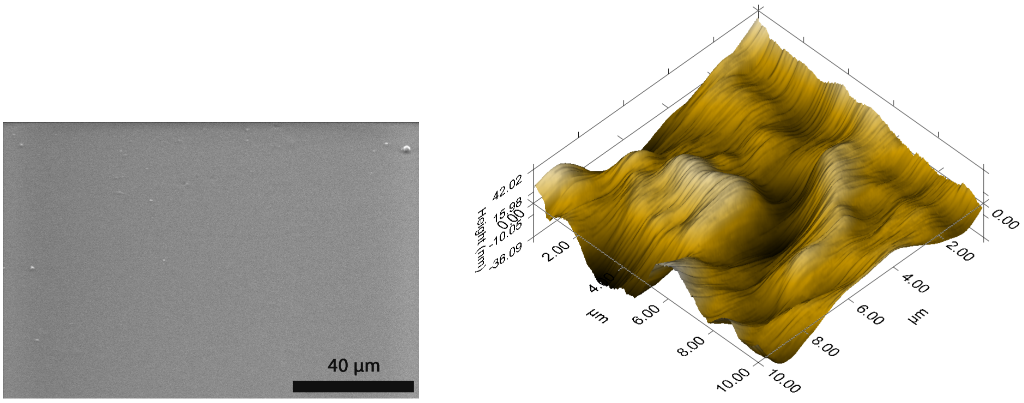

Figure 15: The surface topography of the tested silicone rubber: 2D surface by scanning electron microscopy (left), 3D topography from In-Situ SPM imaging mode using a Berkovich indentation tip (right)

The nanoindentation experiments[2] have been performed on a TI 900 TriboIndenter® of Hysitron Inc., MN, USA. In the present study, all experiments have been performed in a quasi-static process by either closed-loop force or displacement controlled mode with peak values of 50 μN or 3000 nm, respectively. As shown in Fig. 16 (left) and Fig. 17 (left), a holding step of constant displacement or force is added between the loading and unloading step. The relaxation of the applied force as well as the deformation creep can be observed in the holding stage. The resulting observations are distinctive evidences for the viscoelastic behavior of the investigated material. The relaxation protocol uses the described load function in displacement controlled mode with a holding step lasting for 60 s at the peak displacement of 3000 nm. The loading and unloading steps were performed in 20 s, respectively. At the end of the experiment, a negative force value is observed even for zero displacement. This phenomenon is

---

[1] The surface scanning was performed using the device in Leibniz Institute for New Materials, Saarbrücken, Germany

[2] The nanoindentation experiments were performed using the device of the Chair of Material Science and Methodology at Saarland University under the direction of Prof. H. Vehoff.

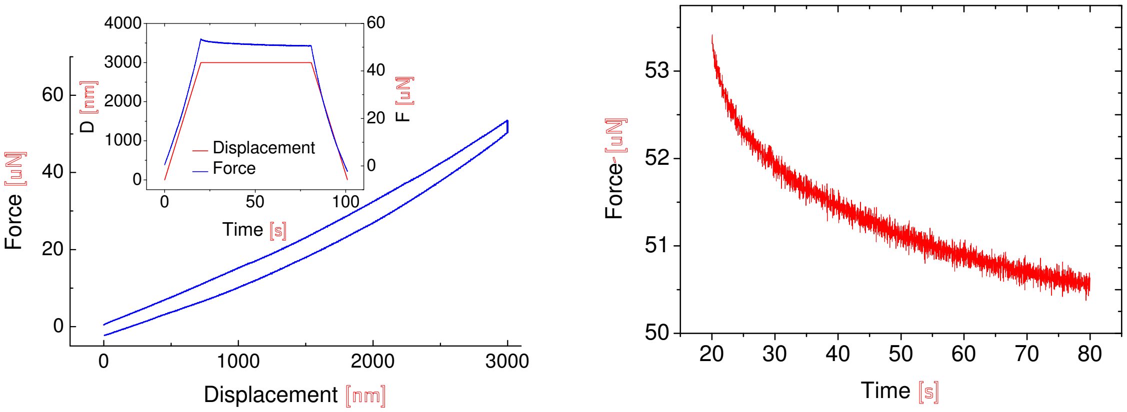

Figure 16: The force-displacement curves of nanoindentation experiments on silicone rubber using the relaxation testing protocol: Force-displacement curve (left), Relaxation behavior (right)

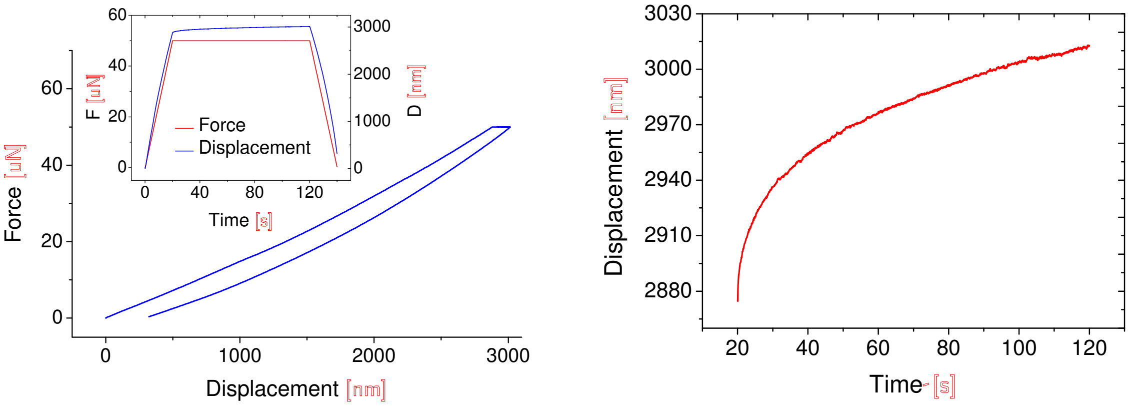

Figure 17: The force-displacement curves of nanoindentation experiments on silicone rubber using the creep testing protocol: Force-displacement curve (left), Creep behavior (right)

an evidence that adhesion is present during the indentation process (Cao et al., 2005; Carrillo et al., 2005; Liao et al., 2010; Cakmak et al., 2012). Fig. 16 (right) only presents the relaxation behavior of the experiment. The force relaxes 6% with respect to the maximum force within 60 s towards the equilibrium state. Fig. 17 demonstrates the creep behavior of the material. The force is ramped to the peak force of 50 μN in 20 s. Subsequently it is reduced to zero with the same rate after holding the peak force for 100 s. In the force-displacement curve, it is obvious that the residual displacement is comparably large. The reasons may be viscous dissipation as well as adhesion effects (Gupta et al., 2007; Cakmak et al., 2012; Charitidis, 2011). The displacement increases about 5% during the holding step and could reach the equilibrium state if the holding time would be long enough. Consequently, it is possible to simultaneously identify the viscoelastic behavior and the adhesion effect from the force-displacement data of the nanoindentation experiments. The other type of loading history is the monotonic testing protocol, in which a stepwise ramping to the peak load or displacement is created by alternating loading and holding steps, c. f. Fig. 18. It is followed by a stepwise decrease back to zero using the same steps. Displacement control mode uses a loading and unloading rate of 200 nm/s and shows holding steps at 1000 nm, 2000 nm and 3000 nm, while in force control mode the steps are performed at 20 N, 30 N, 40 N and 50 N with rates of 2 N/s. All holding steps last for 20 s. As shown in Fig. 18 (left), if the displacement is held constant, the force relaxes during the loading stage but increases during the unloading stage. Similar results are also obtained from the force controlled testing that is presented in Fig. 18 (right). If the holding stage is sufficiently long, the two points should be close to the equilibrium state. The cross point can be considered as the equilibrium point. Usually, if the relaxation time is extra long, the average values of the static states after the relaxation of loading and unloading stages could be considered as approximated equilibrium points. The adhesion effects are shown clearly in both the displacement and the force controlled monotonic force-displacement curves.

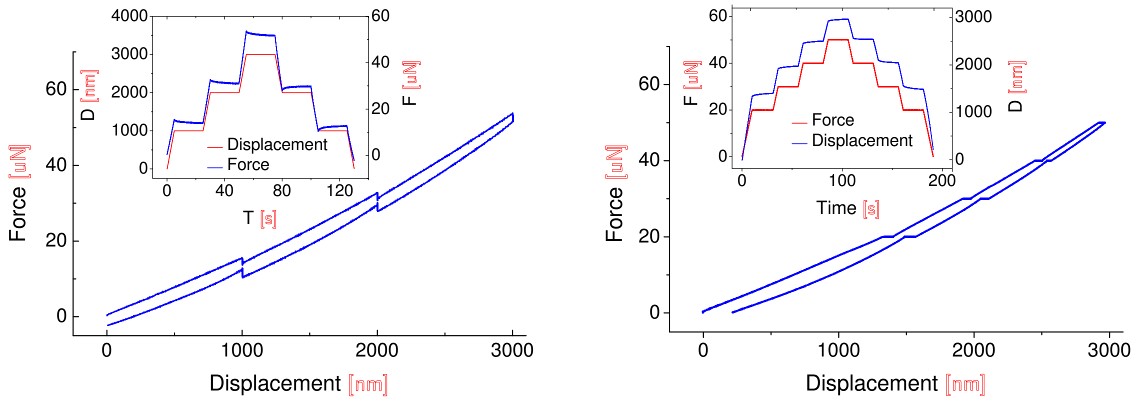

Figure 18: The force-displacement curves of nanoindentation experiments on silicone rubber using the monotonic testing protocol: displacement controlled (DC) (left), load controlled (LC) (right)

4.2 Numerical Modeling

4.2.1 Viscoelastic Model at Finite Deformation

The finite viscoelasticity is characterized explicitly by means of an internal variable model following the concept of Simo (Simo, 1987) and Holzapfel (Holzapfel and Simo, 1996). The internal variables are defined as the stresses $\mathbf{Q}_j$ of the Maxwell elements.
The change of the free energy Ψ within an isothermal viscoelastic process from the reference to the current configuration is given as

$$\Psi(\mathbf{C}, \mathbf{\Gamma_1}...\mathbf{\Gamma_n}) = \Psi^{\infty}_{vol}(J) + \Psi^{\infty}_{iso}(\bar{\mathbf{C}}) + \sum_{j=1}^{n} \Upsilon_j(\bar{\mathbf{C}}, \mathbf{\Gamma}_j). \tag{17}$$

The scalar-valued functions $\Upsilon_j, j = 1, ..., n$ represent the configurational free energy stalled in the springs of the parallel Maxwell elements and define the non-equilibrium state. The free energies Υ_j are functions of the isochoric part of the right Cauchy Green strain tensor $\mathbf{C}$ and of a set of strain-like internal variables $\mathbf{\Gamma}_j, j = 1, ..., n$. The physical expression for the second Piola-Kirchhoff stress $\mathbf{S}$ is in the form

$$\mathbf{S} = 2\frac{\partial\Psi(\mathbf{C}, \mathbf{\Gamma_1}...\mathbf{\Gamma_n})}{\partial\mathbf{C}} = \mathbf{S}^{\infty}_{vol} + \mathbf{S}^{\infty}_{iso} + \sum_{j=1}^{n} \mathbf{Q}_j. \tag{18}$$

Considering the efficient time integration algorithms that are suitable for the finite element procedure, the internal stress tensor variables $\mathbf{Q}_j, j = 1, ..., n$ evolve with a linear equation (for details, please see (Simo, 1987; Holzapfel and Simo, 1996) and (Holzapfel, 2001, Chp. 6))

$$\dot{\mathbf{Q}}_j + \frac{\mathbf{Q}_j}{r_j} = \dot{\mathbf{S}}_{iso\,j}, \qquad j = 1, ..., n, \tag{19}$$

herein, the tensors $\mathbf{S}_{iso\,j}$ characterize the isochoric second Piola-Kirchhoff stresses corresponding to the strain energy $\Psi_{iso\,j}(\bar{\mathbf{C}})$ which is responsible for the j-relaxation process with the relaxation time r_j, $j = 1, ..., n$. According to (Govindjee and Simo, 1992): if a viscoelastic medium such as a thermoplastic elastomer, is composed of identical polymer chains, e. g. silicone rubber, we can assume that $\Psi_{iso\,j}$ is replaceable by Ψ^{∞}_{iso}

$$\Psi_{iso\,j}(\bar{\mathbf{C}}) = \beta^{\infty}_j \Psi^{\infty}_{iso}(\bar{\mathbf{C}}), \qquad j = 1, ..., n, \tag{20}$$

where $\beta^{\infty}_j \in [0, \infty)$ are given as non-dimensional strain-energy factors associated with the relaxation time r_j, $j = 1, ..., n$. Finally, the stresses $\mathbf{S}_{iso\,j}$ can be replaced by $\mathbf{S}^{\infty}_{iso}$ as

$$\mathbf{S}_{iso\,j} = \beta^{\infty}_j \mathbf{S}^{\infty}_{iso}(\bar{\mathbf{C}}), \qquad j = 1, ..., n. \tag{21}$$

The free energy of the neo-Hooke form, which provides a mathematically simple and reliable constitutive model for the non-linear deformation behavior, is chosen to describe the finite elastic response of silicone rubber

$$\Psi(\mathbf{C}) = \Psi^{\infty}_{vol}(J) + \Psi^{\infty}_{iso}(\bar{\mathbf{C}}) = \frac{1}{\mathrm{D}_1}(J-1)^2 + \mathrm{C}_{10}(\bar{I}_1 - 3). \tag{22}$$

The evolution equations in the linear differential form eq. (19) can be solved by an implicit Euler-backward integration scheme. Considering the time interval $[t_n, t_{n+1}]$ we define the time step $\Delta t := t_{n+1} - t_n$. By using the basic approach for a time-dependent variable one obtains the equations for each Maxwell element

$$\mathbf{Q}_j(t_{n+1}) = \beta^{\infty}_j \xi_j \mathbf{S}^{\infty}_{iso}(t_{n+1}) + \mathcal{H}_j(t_n), \qquad j = 1, ..., n, \tag{23}$$

with the definition

$$\xi_j = \frac{r_j}{r_j + \Delta t}, \qquad \mathcal{H}_j(t_n) = \xi_j \Big\{ \mathbf{Q}_j(t_n) - \beta^{\infty}_j \mathbf{S}^{\infty}_{iso}(t_n) \Big\}, \qquad j = 1, ..., n. \tag{24}$$

4.2.2 FEM Model with Adhesive Contact

In this study, because the silicone rubber is assumed to be isotropic and the Berkovich indentation tip can be represented by an effective conical indenter with a half angle of 70.3°, an axisymmetric 2D FE model is applied in ABAQUS®. The real geometry of the indenter tip is taken into account. Firstly, the shape of the Berkovich tip is scanned in 3D by the In-Situ SPM imaging mode stalled in the TriboIndenter®, as shown in Fig. 19 (left). The effective conical edge is combined with the tip curvature by the smooth transition technique as illustrated in Fig. 19 (right). Hence, the Berkovich indenter is simulated by an effective conical indenter with the real shape tip, which is a spherical curve with a radius of 15.63 μm as shown in Fig. 19 (right). For the FE model, the tip can be assumed to be a rigid body compared to the soft polymer. The geometrical size of the polymer sample is 200 μm $\times$ 200 μm. Similar to the model in Section 3, considering the silicone rubber in the study as an incompressible material, the linear axisymmetric 4-node hybrid element type CAX4H in ABAQUS/Standard is chosen. For each studied configuration, the mesh convergence is checked by more than 100000 degrees of freedom. It shows that a coarser mesh, consisting of at least 10000 degrees of freedom, can give converged results.

Concerning the numerical treatment of the contact problem, a contact pair is formed with the tip as the master surface and the layer as the slave surface. In this study, because the ratio of the indentation depth to the layer thickness is smaller than 1%, friction is negligible according to numerical results of our previous work (Chen et al., 2011). Hence, here we only focus on the normal contact. The default contact pressure-clearance relationship used in ABAQUS®/Standard is referred as the ”hard” contact model. In this case, the formulation of the normal contact is used as a constraint for non-penetration, which treats the normal contact as an unilateral constraint problem. It only transmits pressure once the surfaces are in contact within a contact zone c, as shown in Fig. 20 (left). However, this interaction model is not sufficient to simulate the real experimental behavior as adhesion is not taken into account. As a result, an adhesion zone is added to the contact zone forming an interaction area of radius $c + a$. The adhesive behavior is implemented as an interaction of the contact pair. It is defined as a surface-based cohesive behavior in ABAQUS® with a traction-separation relationship as shown in Fig. 20 (right), which assumes initially linear elastic behavior followed by the initiation and the evolution of damage. The elastic behavior is written in terms of an adhesive stiffness $\mathbf{K} = [K_{nn}, K_{ss}, K_{tt}]^T$ that relates the stresses to the separation at the

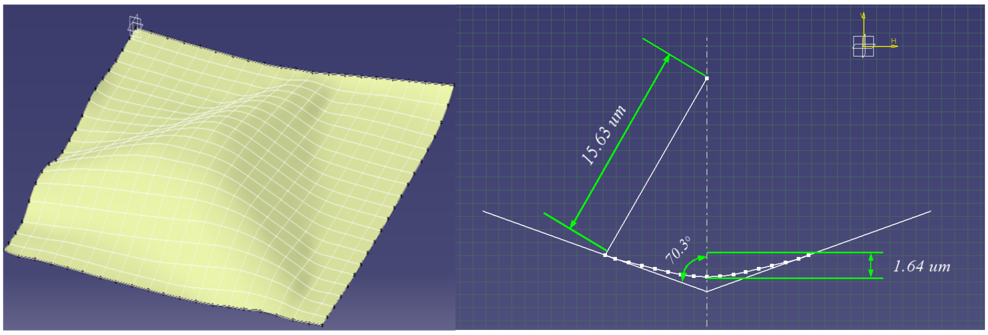

Figure 19: 3D scanning image of the tip shape geometry (left) and the 2D effective conical indenter with a spherical tip that originated from the 3D scanning data (right)

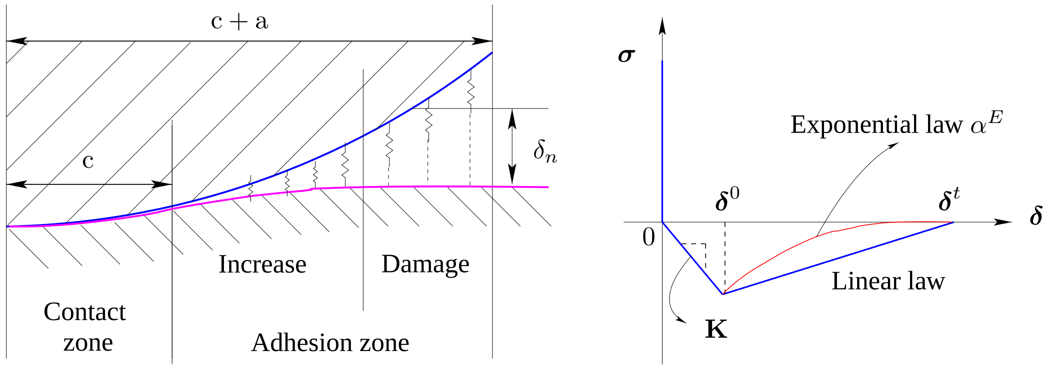

Figure 20: Adhesive contact Geometry (left), Traction-separation relationship with a linear or exponential damage evolution law in adhesive contacts (right)

damage initiation $\boldsymbol{\delta}^0 = [\delta^0_{nn}, \delta^0_{ss}, \delta^0_{tt}]^T$ across the interface. The process of degradation begins when the contact separation satisfies a certain damage initiation criteria related to $\boldsymbol{\delta}^0$. A linear or exponential damage evolution law describes the rate at which the adhesive stiffness **K** is degraded once the corresponding initiation criterion is reached. The evolution laws are defined with a separation at the complete failure δ^t_{nn} and the non-dimensional exponential parameter α^E.

4.3 Identification Results

The experimental results of silicone rubber only show slight viscoelastic behavior in both the relaxation and the creep tests. Therefore, two Maxwell-elements are expected to sufficiently represent the relaxation spectrum. It is assumed that the separation is the same for all three directions at the initial damage, in order to simplify the identification of the adhesive model. Not only the linear, but also the exponential evolution laws of damage are taken into account in the model. The force-displacement data of the relaxation in displacement controlled mode are used as the reference data in the identification. Several identification procedures with different initial parameter sets lead to almost the same final optimized values. Therefore, a valid minimum is obtained according to the objective function. The reproducibility of the nanoindentation experimental data in this study are good and the maximum deviation between the three repeated experiments is less than 4.5%. It is recognized that if the noise is less than 5% of the data, the identified results are not sensitive to the data noise (Chen and Diebels, 2012).

Table 5: The identified model parameters with a linear and exponential evolution law

Linear Evolution Law for Adhesive Damage					
C_{10}(MPa)	D_1	β_1^∞	r_1(s)	β_2^∞	r_2(s)
0.16714	0.00486	0.11465	0.10176	0.05098	8.06892
$K_{nn}(\frac{\mu N}{\mu m^3})$	$K_{ss}(\frac{\mu N}{\mu m^3})$	$K_{tt}(\frac{\mu N}{\mu m^3})$	$\delta^0_{nn}(\mu m)$	$\delta^t_{nn}(\mu m)$	
0.01021	0.17722	0.03147	0.31996	10.44223	
Exponential Evolution Law for Adhesive Damage					
C_{10}(MPa)	D_1	β_1^∞	r_1(s)	β_2^∞	r_2(s)
0.16770	0.00533	0.10286	0.11330	0.04822	6.21961
$K_{nn}(\frac{\mu N}{\mu m^3})$	$K_{ss}(\frac{\mu N}{\mu m^3})$	$K_{tt}(\frac{\mu N}{\mu m^3})$	$\delta^0_{nn}(\mu m)$	$\delta^t_{nn}(\mu m)$	α^E
0.010531	0.17054	0.08865	0.41149	9.65793	7.25348

As shown in Table 5, C_{10} is responsible for the equilibrium isochoric hyperelastic behavior and results in approximately the same value, regardless if the linear or the exponential evolution law is considered. The compressibility parameter D_1 is found to be about 0.005, which demonstrates that the silicone rubber is nearly incompressible. The small relaxation times r_1 and r_2 for the two Maxwell elements represent the slight rate-dependent behavior of the silicone rubber in nanoindentation experiments. The identified adhesive stiffness **K** as illustrated in Fig. 20 (right) is the same for the linear evolution law and the exponential law. At the point of damage initiation, the separation is around 300 nm or 400 nm for the linear or the exponential evolution law, respectively, while the distance at

complete failure is in the range of 10 μm in both adhesive models. As expected, the identification of the material parameters are independent on the used evolution law in the adhesive contact model.
Fig. 21 and Fig. 22 present the comparisons between the experimental data and numerical prediction using the parameters that are identified by the indentation response. The numerical simulations on the left side and the right side of Fig. 21 and Fig. 22 are performed using the linear evolution law and exponential law of the adhesive contact model with the identified parameters in Table 5, respectively. All comparisons indicate that there is a good agreement between the experimental measurements and the numerical simulation. The relaxation and creep processes in the cyclic or monotonic holding stages are accurately predicted by the numerical simulations for nanoindentation experiments. As a conclusion, it can be argumented that the viscoelastic behavior of the silicone rubber can be characterized by the chosen constitutive model together with the identified parameters from nanoindentation experiments. Adhesion effects, namely a negative force at zero displacement as well as a residual displacement after withdrawing the indenter, are also accurately calculated by the numerical simulation. Hence, the adhesive contact model illustrated in Fig. 20 can be used to quantify these adhesion effects in nanoindentation experiments. The simulation results using either a linear or exponential evolution law for the adhesive contact show no significant difference.

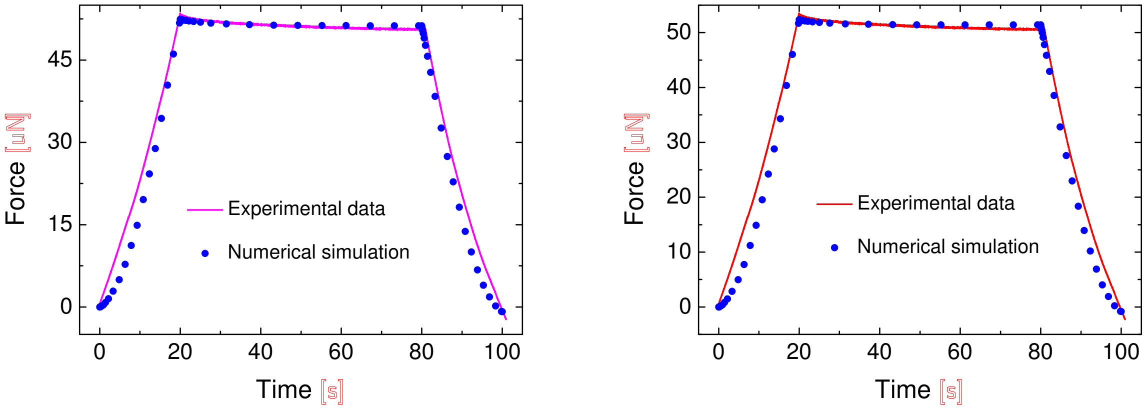

Figure 21: Relaxation tests: Linear evolution law (left), Exponential evolution law (right)

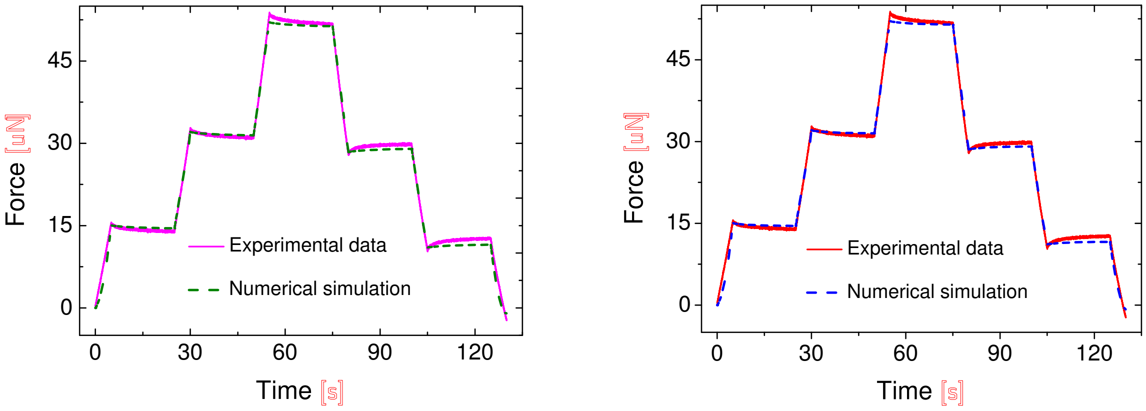

Figure 22: Monotonic relaxation tests: Linear evolution law (left), Exponential evolution law (right)

5 Conclusion and Outlook

In the present work, an analysis procedure to characterize polymers from nanoindentation has been developed using the FEM based inverse method. The developed inverse procedure has been sufficiently applied to identify the hyperelastic as well as viscoelastic properties of polymers with the concept of parameters re-identification, in which the identified results are able to be quantified. The surface roughness effects have been investigated numerically by explicitly taking into account the roughness profile in the model. The influence of the surface roughness is quantified as a function of the sine parameters as well as of the indentation parameters. Finally, this inverse procedure is extended to use in the real nanoindentation. The viscoelastic behavior of silicone rubber in nanoindentation is described with a viscoelastic model at finite deformation taking into account the adhesion effects. The parameters of the viscoelastic constitutive model as well as the adhesive contact model are able to be identified simultaneously from nanoindentation using the FEM based inverse procedure.

As for the future work, firstly, it is meaningful to quantify the influence of surface roughness on the force-displacement data in a more explicit way, which is practical to apply into the experiment or numerical computation as a calibration source. Secondly, comparing work has to be done in order to verify the ability to characterize polymers from nanoindentation. One comparison will be made between the characterization of polymers from indentation performed on different scales, i. e. macro- and nanoindentation, leading to a quantification of the effects related to adhesion and surface roughness, which are sensitive in nanoscale but unimportant in macro-scale. This part of work will be included in the upcoming paper. Thirdly, nanoindentation experiments are typically carried out on multiple spatial scales, i. e. atomic-scale, nanoscale, microscale and continuum scale. In this case, multiscale simulations combining the greatest advantage of both atomistic and FEM simulations have to be developed in the field of nanoindentation of polymers. Therefore, multiscale simulation from atomistic simulation to finite element computation is our next key task in the research field on nanoindentation of polymers.

Acknowledgments

The authors are grateful to the DFG (German Science Foundation—Deutsche Forschungsgemeinschaft) for financial support through the grant number Di 430/14.

References

Benedix, U.; Goerke, U.; Kreissig, R.; Kretzschmar, S.: Local and global analysis of inhomogeneous displacement fields for the identification of material parameters. In: *Proceedings of the International Conference on Computer Methods in Composite Materials, CADCOMP*, pages 159–168 (1998).

Berke, P.; Houdaigui, F. E.; Massart, T. J.: Coupled friction and roughness surface effects in shallow spherical nanoindentation. *Wear*, 268, (2010), 223–232.

Bobji, M. S.; Shivakumar, K.; Alehossein, H.; Venkateshwarlu, V.; Biswas, S. K.: Influence of surface roughness on the scatter in hardness measurements-a numerical study. *Int. J. Rock Mech. Min. Sci.*, 36, (1999), 399–404.

Bolzon, G.; Maier, G.; Panico, M.: Material model calibration by indentation, imprint mapping and inverse analysis. *Int. J. Solids Structures*, 41, (2004), 2957–2975.

Bouzakis, K. D.; Michailidis, N.; Hadjiyiannis, S.; Skordaris, G.; Erkens, G.: The effect of specimen roughness and indenter tip geometry on the determination accuracy of thin hard coatings stress-strain laws by nanoindentation. *Materials Characterization*, 49, (2003), 149–156.

Cakmak, U. D.; Schöberl, T.; Major, Z.: Nanoindentation of polymers. *Arch. Rat. Mech. Anal.*, 42, (2012), 707–718.

Cao, Y.; Yang, D.; Soboyejoy, W.: Nanoindentation method for determining the initial contact and adhesion characteristics of soft polydimethysiloxane. *J. Mater. Res.*, 20, (2005), 2004–2011.

Carrillo, F.; Gupta, S.; Balooch, M.; Marshall, S. J.; Marshall, G. W.; Pruitt, L.; Puttlitz, C. M.: Nanoindentation of polydimethylsiloxane elastomers: Effect of crosslinking, work of adhesion, and fliud environment on elastic modulus. *J. Mater. Res.*, 20, (2005), 2820–2830.

Charitidis, C.: Nanoscale deformation and nanomechanical properties of soft matter study cases: Polydimethylsiloxane, cells and tissues. *ISRN Nanotechnology*, doi:10.5402/2011/719512, (2011), 1–13.

Chen, Z.; Diebels, S.: Nanoindentation of hyperelastic polymer layers at finite deformation and parameter re-identification. *Arch. Appl. Mech.*, 82, (2012), 1041–1056.

Chen, Z.; Diebels, S.; Schmitt, J.: Frictional nanoindentation of hyperelastic polymer layers: A numerical study. *Proceedings of the* 3^{rd} *ECCOMAS Thematic Conference on the Mechanical Response of Composites*, pages 229–236.

Deb, K.: An efficient constraint handling method for genetic algorithms. *Computer Methods in Applied Mechanics and Engineering*, 186, (2000), 311–338.

Deuschle, J.: *Mechanics of soft polymers indentation*. Doctoral Thesis, Universität Stuttgart (2008).

Donnelly, E.; Baker, S. P.; Boskey, A. L.; van der Meulen, M. C. H.; Biomed, J.: Effects of surface roughness and maximum load on the mechanical properties of cancellous bone measured by nanoindentation. *Journal of Biomedical Materials Research - Part A*, 77, (2006), 426–435.

Fischer-Cripps, A. C.: *Nanoindentation*. Springer, New York (2004).

Giannakopoulos, A. E.; Panagiotopoulos, D. I.: Conical indentation of incompressible rubber-like material. *Int. J. Solids Structures*, 46, (2009), 1436–1447.

Giannakopoulos, A. E.; Triantafyllou, A.: Spherical indentation of incompressible rubber-like material. *J. Mech. Phys. Solids*, 55, (2007), 1196–1211.

Goffe, W. L.; Ferrier, G. D.; Rogers, J.: Global optimization of statistical functions with simulated annealing. *Journal of Econometrics*, 60, (1994), 65–99.

Govindjee, S.; Simo, J. C.: Mullins effect and the strain amplitude dependence of the storage modulus. *Int. J. Solids Structures*, 29, (1992), 1737–1751.

Guessasma, S.; Sehaki, M.; Lourdin, D.; Bourmaud, A.: Viscoelasticity properties of biopolymer composite material determined using finite element calculation and nanoindentation. *Comp. Mat. Science*, 44, (2008), 371–377.

Gupta, S.; Carrillo, F.; Li, C.; Pruitt, L.; Puttlitz, C.: Adhesive forces significantly affect elastic modulus determination of soft polymeric materials in nanoindentation. *Materials Letters*, 61, (2007), 448–451.

Hartmann, S.: Computation in finite-strain viscoelasticity: finite elements based on the interpretation as differential-algebraic equations. *Comp. Meth. Appl. Mech. Eng.*, 191, (2002), 1439–1470.

Hartmann, S.; Gibmeier, J.; Scholtes, B.: Experiments and material parameter identification using finite elements. uniaxial tests and validation using instrumented indentation tests. *Exp. Mech.*, 46, (2006), 5–18.

Hartmann, S.; Haupt, P.; Tschöpe, T.: Parameter identification with a direct search method using finite elements. *D. Besdo & R. H. Schuster & J. Ihlemann: Constitutive Models for Rubber II, Balkema Publ., Lisse*, 249–256.

Hartmann, S.; Tschöpe, T.; Schreiber, L.; Haupt, P.: Finite deformations of a carbon black-filled rubber. Experiment, optical measurement and material parameter identification using finite elements. *Eur. J. Mech., A/Solids*, 22, (2003), 309–324.

Heimes, T.: Finite Thermoinelastizität: Experimente, Materialmodellierung und Implementierung in die FEM am Beispiel einer technischen Gummimischung. In: Fortschritt-Berichte // VDI / Reihe 5, Grund- und Werkstoffe, Kunststoffe: 709, VDI-Verlag, (2005).

Holzapfel, G. A.: On large strain viscoelasticity: Continuum formulation and finite element applications to elastomeric structures. *Int. J. Numer. Meth. Eng.*, 39, (1996), 3903–3926.

Holzapfel, G. A.: *Nonlinear solid mechanics: A continuum approach for engineering*. John Wiley & Sons, Chichester (2001).

Holzapfel, G. A.; Simo, J. C.: A new viscoelastic constitutive model for continuous media at finite thermomechanical changes. *Int. J. Numer. Meth. Eng.*, 33, (1996), 3019–3034.

Huber, N.; Nix, W. D.; Gao, H.: Identification of elastic-plastic material parameters from pyramidal indentation of thin films. *Proc. R. Soc. Lond. A*, 458, (2002), 1593–1620.

Huber, N.; Tsakmakis, C.: Finite deformation viscoelasticity laws. *Mech. Mater.*, 32, (2000), 1–18.

Huber, N.; Tyulyukovskiy, E.: A new loading history for identification of viscoplastic properties by spherical indentation. *J. Mater. Res.*, 19, (2004), 101–113.

Jiang, W. G.; Su, J. J.; Feng, X. Q.: Effect of surface roughness on nanoindentation test of thin films. *Eng. Fract. Mech.*, 75, (2008), 4965–4972.

Johlitz, M.; Diebels, S.: Characterisation of a polymer using biaxial tension tests. part I: Hyperelasticity. *Arch. Appl. Mech.*, 81, (2011), 1333–1349.

Johnson, K. L.: *Contact mechanics*. Cambridge University Press, Cambridge (1985).

Kaliske, M.; Rothert, H.: Formulation and implementation of three-dimensional viscoelasticity at small and finite strains. *Comp. Mech.*, 19, (1997), 228–239.

Kirkpatrick, S.; Gelatt Jr., C. D.; Vecchi, M. P.: Optimization by simulated annealing. *Science*, 220, (1983), 671–680.

Klötzer, D.; Ullner, C.; Tyulyukovskiy, E.; Huber, N.: Identification of viscoplastic material parameters from spherical indentation data. part II: Experimental validation of the method. *J. Mater. Res.*, 21, (2006), 677–684.

Krämer, S.; Rothe, S.; Hartmann, S.: Homogeneous stress-strain states computed by 3d-stress algorithms of fe-codes: application to material parameter identification. *Engineering with Computers*, pages DOI: 10.1007/s00366–013–0337–7.

Kreissig, R.: Analysis of inhomogeneous displacement fields for the parameter identification of elastic-plastic deformation laws. *Forschung im Ingenieurwesen/Engineering Research*, 64, (1998), 99–109.

Kreissig, R.; Benedix, U.; Grke, U. .: Statistical aspects of the identification of material parameters for elasto-plastic models. *Arch. Appl. Mech.*, 71, (2001), 123–134.

Kumar, A. K. N.; Kannan, M. D.; Jayakumar, S.; Rajam, K. S.; Raju, V. S.: Investigations on the mechanical behaviour of rough surfaces of TiNi thin films by nanoindentation studies. *Surf. Coat. Technol.*, 201, (2006), 3253–3259.

Lagarias, J. C.; Reeds, J. A.; Wright, M. H.; Wright, P. E.: Convergence properties of the nelder-mead simplex method in low dimensions. *SIAM Journal on Optimization*, 9, (1999), 112–147.

Lawitts, J. A.; Biggers, J. D.: Optimization of mouse embryo culture media using simplex methods. *Journal of reproduction and fertility*, 91, (1991), 543–556.

Le Saux, V.; Macro, Y.; Bles, G.; Calloch, S.; Moynea, S.; Plessisa, S.; Charrierb, P.: Identification of constitutive model for rubber elasticity from micro-indentation tests on natural rubber and validation by macroscopic tests. *Mech. Mater.*, 43, (2011), 775–786.

Liao, Q.; Huang, J.; Zhu, T.; Xiong, C.; Fang, J.: A hybrid model to determine mechanical properties of soft polymers by nanoindentation. *Thin Solid Films*, 16, (2010), 1043–1047.

Lion, A.: A constitutive model for carbon black filled rubber: Experimental investigations and mathematical representation. *Continuum Mech. Therm.*, 8, (1996), 153–169.

Lion, A.: Thixotropic behaviour of rubber under dynamic loading histories: Experiments and theory. *J. Mech. Phys. Solids*, 46, (1998), 895–930.

Lubliner, J.: A model of rubber viscoelasticity. *Mech. Res. Commun.*, 12, (1985), 93–99.

Mahnken, R.: Identification of material parameters for constitutive equations. *Int. J. Solids Structures*, 2, (2004), 637–655.

Mahnken, R.; Stein, E.: The identification of parameters for visco-plastic models via finite-element methods and gradient methods. *Modelling and Simulation in Materials Science and Engineering*, 2, (1994), 597–616.

Marckmann, G.; Verron, E.: Comparison of hyperelastic models for rubber-like materials. *Rubber Chem. Technol.*, 79, (2005), 835–858.

Mata, M.; Alcalá, J.: The role of friction on sharp indentation. *J. Mech. Phys. Solids*, 455, (2004), 145–165.

Miller, M.; Bobko, C.; Vandamme, M.; Ulm, F. J.: Surface roughness criteria for cement paste nanoindentation. *Cement and Concrete Research*, 38, (2008), 467–476.

Mooney, M.: A theory of large elastic deformation. *J. Appl. Phys.*, 11, (1940), 582–592.

Oliver, W. C.; Pharr, G. M.: An improved technique for determining hardness and elastic modulus using load and displacement sensing indentation experiments. *J. Mater. Res.*, 7, (1992), 1564–1583.

Oliver, W. C.; Pharr, G. M.: Measurement of hardness and elastic modulus by instrumented indentation: Advance in understanding and refinements to methodology. *J. Mater. Res.*, 19, (2004), 3–20.

Rauchs, G.: Optimization-based material parameter identification in indentation testing for finite strain elasto-plasticity. *Z. Angew. Math. Mech.*, 86, (2006), 539–562.

Rauchs, G.; Bardon, J.: Identification of elasto-viscoplastic material parameters by indentation testing and combined finite element modelling and numerical optimization. *Finite Elem. Anal. Des.*, 47, (2011), 653–667.

Rauchs, G.; Bardon, J.; Georges, D.: Identification of the material parameters of a viscous hyperelastic constitutive law from spherical indentation tests of rubber and validation by tensile tests. *Mech. Mater.*, 42, (2010), 961–973.

Rivlin, R. S.: Large elastic deformations of isotropic materials. iv. further developments of the general theory. *Phil. Trans. Roy. Soc. Lond A*, A241, (1948), 379–397.

Schwefel, H. P.: *Evolution and optimum seeking*. Wiley, New York (1995).

Simo, J. C.: On a fully three-dimensional finite-strain viscoelastic damage model: Formulation and computational aspects. *Computer Methods in Applied Mechanics and Engineering*, 60, (1987), 153–173.

Simo, J. C.; Taylor, R. L.: Penalty function formulations for incompressible nonlinear elastostatics. *Comp. Meth. Appl. Mech. Eng.*, 35, (1982), 107–118.

Tyulyukovskiy, E.; Huber, N.: Identification of viscoplastic material parameters from spherical indentation data. part I: Neural networks. *J. Mater. Res.*, 21, (2006), 664–676.

Tyulyukovskiy, E.; Huber, N.: Neural networks for tip correction of spherical indentation curves from bulk metals and thin metal films. *J. Mech. Phys. Solids*, 55, (2007), 391–418.

Walter, C.; Antretter, T.; Daniel, R.; Mitterer, C.: Finite element simulation of the effect of surface roughness on nanoindentation of thin films with spherical indenter. *Surf. Coat. Technol.*, 202, (2007), 1103–1107.

Walter, C.; Mitterer, C.: 3d and 2d finite element simulation of the effect of surface roughness in nanoindentation of hard coatings. *Surf. Coat. Technol.*, 203, (2008), 3286–3290.

Wriggers, P.: *Computational Contact Mechanics*. Springer-Verlag, Berlin (2006).

Yeoh, O. H.: Characterization of elastic properties of carbon-black-filled rubber vulcanizates. *Rubber Chem. Technol.*, 55, (1990), 792–805.

Address: Chair of Applied Mechanics, Saarland University, PO Box 151150, 66041 Saarbrücken, Germany
email: `zh.chen@mx.uni-saarland.de (Z. Chen),`
`s.diebels@mx.uni-saarland.de (S. Diebels)`